NAM

# Kinematic modelling of large tremors in the Groningen field using extended seismic sources
# Huizinge Earthquake Part 2

**Shell Global Solutions**

**H.M. Wentinck**

Datum July 2018

Editors Jan van Elk, & Dirk Doornhof

## General Introduction

The Huizinge earthquake of 16th August 2012 with a magnitude of $M_L$ = 3.6 had a profound impact on the Groningen community and led to the acceleration of the research program into induced seismicity in Groningen. As part of this program new capabilities were developed. For instance, geomechanical modelling of rupture processes taking place in the depleted gas reservoir of the Rotliegend formation was improved.

Using these capabilities, the Huizinge earthquake of 2012 was revisited (Ref. 1). A report from 2017 (Ref. 1) describes the estimation of rupture dimensions based on the surface recording of the earthquake using kinematic modelling of the earthquake. The current report is an extension of this work.

## References

1. Kinematic modelling of large tremors in the Groningen field using extended seismic sources – Huizinge Earthquake Part 1, SGS, H.M. Wentinck, August 2017

NAM

| | | | | |
|---|---|---|---|---|
| **Title** | **Kinematic modelling of large tremors in the Groningen field using extended seismic sources Huizinge Earthquake Part 2** | | **Date** | July 2018 |
| | | | **Initiator** | NAM |
| **Author(s)** | H.M. Wentinck | **Editor** | Jan van Elk and Dirk Doornhof | |
| **Organisation** | SGS (Shell) | **Organisation** | NAM | |
| **Place in the Study and Data Acquisition Plan** | Study Theme: Geomechanical Modelling<br>Comment:<br>The Huizinge earthquake of 16th August 2012 with a magnitude of $M_L$ = 3.6 had a profound impact on the Groningen community and led to the acceleration of the research program into induced seismicity in Groningen. As part of this program new capabilities were developed. For instance, geomechanical modelling of rupture processes taking place in the depleted gas reservoir of the Rotliegend formation was improved.<br>Using these capabilities, the Huizinge earthquake of 2012 was revisited (Ref. 1). A report from 2017 describes the estimation of rupture dimensions based on the surface recording of the earthquake using kinematic modelling of the earthquake. The current report is an extension of this work. | | | |
| **Directly linked research** | 1. Reservoir engineering studies in the pressure depletion for different production scenarios.<br>2. Seismic monitoring activities; both the extension of the geophone network and the installation on geophones in deep wells.<br>3. Geomechanical studies<br>4. Subsidence and compaction studies. | | | |
| **Used data** | KNMI Earthquake catalogue<br>Geological maps of faults in the Rotliegend reservoir | | | |
| **Associated organisation** | | | | |
| **Assurance** | | | | |

**report for NAM 2018**

# Kinematic modelling of large tremors in the Groningen field using extended seismic sources

## second results related to the Huizinge 2012 tremor

**by**

**H.M. Wentinck**

## Executive Summary

This work is about the kinematic modelling of the relatively large Huizinge tremor of 2012 in the Groningen field and is a continuation of the work reported in Wentinck (2017). Compared with the first report, the signals of three other KNMI ground accelerometers near the epicentre of the Huizinge tremor have been included.

The comparison between simulated and observed signals is complicated because the orientations of the ground accelerometers in the horizontal plane is unknown. So far, the orientations have been reconstructed from searching for a maximal radial energy during the passage of the P wave. To verify this method, recordings have been studied of several other recent tremors in the Groningen field by KNMI seismometer stations with both downhole geophones and ground accelerometers.
These recordings show that this method is questionable. While practically all downhole geophone signals show maximal radial energy during the passage of the P wave, there are often remarkable deviations from this behaviour for the ground accelerometers.

Lacking a robust method to reconstruct the orientations of the ground accelerometers that recorded the Huizinge tremor, we have used another method to derive the seismic source parameters. This method uses that the vertical displacement and the magnitude of the horizontal displacements do not change when the ground accelerometers are rotated in the horizontal plane. Furthermore, we have assumed that the slip plane of the tremor coincides with one of the two faults which have been identified by EBN from ant-tracking and that the tremor hypocentre is located in the reservoir at 3 km depth.

Under these assumptions, ground displacements from the simulations have been compared with the observed ones for both faults by varying the slip direction as the remaining unknown seismic source parameter. This has been done for all six ground accelerometers near the tremor epicentre. The fault which slipped seems to be fault A in NNW - SSE direction with the slip of the hanging wall predominantly downwards. This conclusion is based on a few prominent features in the signals which are invariant under the horizontal rotation of the ground accelerometers.

The multiple (or second observed peak) in the horizontal displacements during the passage of the S wave, such as for the BMD1 station at Middelstum, is not observed at all stations. So far, the simulations indicate that the second peak is not a multiple from wave reflections in the deep subsurface. Likely, this multiple follows from S wave reflections in the shallow subsurface. The recent tremors in the Groningen field generate in several cases similar multiples for the ground accelerometers but not for the downhole geophones at 50 - 200 m depth.

# Table of Contents

Table 0.1 : List of frequently used symbols

| Symbol | Property | Unit |
|---|---|---|
| $\boldsymbol{a}$ | displacement acceleration vector | m/s$^2$ |
| $\lvert a_{rad} \rvert$ | maximal mean rms value of the radial component of the accelerations | m/s$^2$ |
| $D$ | relative displacement or slip over a slip plane | m |
| $D$ | damping or isotropic loss factor for attenuation of seismic waves | - |
| $f$ | frequency | Hz |
| $f_c$ | corner frequency in the spectra of the ground motions | Hz |
| $f(t)$ | source time function | - |
| $f$ | magnitude of a point force | N |
| $\boldsymbol{f}$ | force vector | N |
| $l_{DC}$ | arm of the double couple | m |
| $L$ | length of rupture plane along fault strike | m |
| $M$ | moment magnitude | Richter |
| $\mathrm{M_L}$ | local magnitude | Richter |
| $\boldsymbol{m}$ | moment tensor defining the slip plane orientation and slip direction | - |
| $\boldsymbol{M}$ | moment tensor | Nm |
| $M_0$ | seismic moment | Nm |
| $n$ | shape parameter of modified source time function | - |
| $\boldsymbol{n}$ | unit vector normal to the slip plane | - |
| $Q$ | quality factor for attenuation of seismic waves | m |
| $s$ | distance between seismic source and receiver | m |
| $s_h$ | distance between tremor epicentre and receiver | m |
| $S$ | surface area of rupture plane | m$^2$ |
| $t$ | time | s |
| $t_{nucl}$ | time of nucleation of the rupture | s |
| $t_{onset}$ | onset time of source time function | s |
| $t_r$ | rise time of source time function | s |
| $t_R$ | duration of the rupture in the slip plane | s |
| $t_{trigger}$ | trigger time of a point force of an extended source | s |
| $\Delta t_{ps}$ | time difference between the arrivals of primary and secondary waves | s |
| $\boldsymbol{u}$ | displacement vector | m |
| $V_p$ | velocity of primary wave | m/s |
| $V_s$ | velocity of secondary wave | m/s |
| $V_r$ | rupture velocity | m/s |
| $V_{r,strike}$ | rupture velocity along fault strike | m/s |
| $\boldsymbol{v}$ | displacement velocity vector | m/s |
| $W$ | width of rupture plane along fault dip | m |
| $\boldsymbol{x}$ | Cartesian coordinates of the receiver (or location in the field) | m |
| $x, y, z$ | coordinates used for the analytical solutions | m |
| $X, Y, Z$ | coordinates based on the Dutch Rijksdriehoeksstelsel | m |

Table 0.2 : List of frequently used symbols, continued

| Symbol | Property | Unit |
|---|---|---|
| $\delta$ | dip angle of fault | degree/radian |
| $\delta_{ij}$ | Kronecker delta function | - |
| $\Delta\tau$ | breakdown stress drop over fault plane during rupture | Pa |
| $\Delta_{PS}$ | time difference between arrivals of P and S waves | s |
| $\zeta$ | damping or isotropic loss factor for the attenuation of seismic waves | - |
| $\boldsymbol{\zeta}$ | Cartesian coordinates of the source | m |
| $\lambda$ | wavelength | m |
| $\lambda$ | rake angle of slip vector | degree/radian |
| $\rho$ | mass density of rock | kg/m$^3$ |
| $\tau$ | time constant | s |
| $\phi$ | fault strike azimuth angle | degree/radian |
| $\omega$ | angular or circular frequency of a wave | radian/s |

Table 0.3 : List of frequently used symbols, continued

| Symbol | Refers to |
|---|---|
| ..... | ..... |
| subscripts | |
| area | selected region or area |
| arr | arrival time of wave at receiver |
| DC | double couple |
| hor | horizontal component of displacement, velocity or acceleration |
| p | primary or compressive wave |
| rad | radial component of displacement, velocity or acceleration |
| rec | receiver |
| rms | root mean square value |
| s | secondary or shear wave |
| stf | source time function |
| strike | along fault strike |
| tra | transverse component of displacement, velocity or acceleration |
| ver | vertical component of displacement, velocity or acceleration |
| abbreviations | |
| EBN | Energie Beheer Nederland |
| FEM | finite element method |
| KNMI | Koninklijk Nederlands Metereologisch Instituut |
| NAM | Nederlandse Aardolie Maatschappij |
| P | primary wave |
| RD | Dutch Rijksdriehoeksstelsel coordinate system |
| rms | root mean square |
| S | secondary wave |
| SGS-I | Shell Global Solutions International |
| SH | secondary horizontal wave |
| SV | secondary vertical wave |

# Chapter 1

# Introduction

This work is part of an ongoing effort to understand tremors in the Groningen field, their ground motions and effects on buildings. Recent results can be found in reports and presentations of NAM (2015), Stafleu et al. (2016), Bommer et al. (2015), Edwards et al. (2016), Bommer (2016), Burnett (2016) and van Dedem (2016) in relation to ground motion prediction equations (GMPE's), and of Dost and Kraaijpoel (2013), Dost (2016), Burnett (2016), Terrell (2016) and Lawrence et al. (2015) in relation to seismic moment tensor solutions of large tremors and the interpretation of tremors recorded by the down-hole geophones in the Zeerijp and Stedum wells in the Groningen field[1].

In particular, this work continues with the analysis of the Huizinge tremor as reported by Dost and Kraaijpoel (2013) and Wentinck (2017). This tremor occurred at August 16 2012 and had a local magnitude $M_L = 3.4$. One effort addresses the fundamental uncertainty in the horizontal orientations of the ground accelerometers of the KNMI stations in relation to the analysis of the ground motions caused by this tremor. The other effort addresses the multiples in the horizontal displacements during the passage of the S wave, as recorded by a few stations.

To understand the ground motions caused by the Huizinge tremor, we also investigated the ground motions of several recent tremors as recorded by the extended seismometer network of KNMI of the last few years. The new KNMI stations have geophones in a shallow borehole at 50, 100, 150 and 200 m depth and have at the surface a ground accelerometer similar to the ones which recorded the Huizinge tremor. The set-up of these

[1]Seismic moment tensor solutions relate to the so-called focal mechanism of the seismic source. Often, the focal mechanism or moment tensor of the seismic source can be described in terms of the azimuth and dip angles of the slip plane and the slip direction (or so-called rake angle).
When the subsurface has various formations with different wave velocities, advanced calculations are needed to obtain these source parameters from the ground displacements. When the formations are approximately flat around the tremor hypocentre, software for seismology, such as "Cake" from pyrocko.org GFZ-Potsdam (F.R.G.) can be used. This software is used by KNMI. Otherwise, full wave propagation simulations based on finite difference methods are integrated into the inversion methods. This is done by ExxonMobil and Shell.

sensors enables us to follow the waves through the shallow subsurface when reaching the surface.

From these investigations we have developed another method to compare the recordings of the ground accelerometers with simulations. There are few assumptions. The first one is that the slip plane coincides with one of the two faults that intersect each other at the epicentre of the Huizinge tremor as determined by KNMI, see Dost and Kraaijpoel (2013). These two faults have been identified by Kortekaas and Jaarsma (2017) using fault plane tracking algorithms (or ant-tracking) on the seismic data of the Groningen field. The other assumption is that the tremor hypocentre is in the reservoir at about 3 km depth. The kinematic model used is similar to the one described in Wentinck (2017). The ground motion information used is contained in frequencies below 5 Hz.

Chapter 2 presents the field data used. Chapter 3 summarises the set-up of the FEM simulations. Chapter 4 presents the results. A short discussion follows in Chapter 5. Appendix A shows more field and ground accelerometer data, also from some recent tremors. Appendix B gives some details of the seismic source implemented in the FEM simulations.

# Chapter 2

# Field data used

Figure 2.1 shows two maps of the faults around the epicentre (red dot) of the Huizinge tremor and the locations of the six ground accelerometers used (blue dots). The top figure shows the major faults in the field from the NAM fault database used for reservoir flow modelling and geomechanical calculations. The bottom figure shows more faults in the field and shows that the Huizinge tremor epicentre location coincides with the junction of two faults $A$ and $B$ with little throw. Recently, they have been found by Kortekaas and Jaarsma (2017) using fault plane tracking algorithms (or ant-tracking in Petrel$^{\text{TM}}$) on the seismic data of the Groningen field.
Fault $A$ has fault strike azimuth and fault dip angles $\phi \sim 330°$ and $\delta \sim 68°$, respectively[1]. These values are close to the values proposed by KNMI and which have been used in Wentinck (2017). They are $\phi \sim 320°$, $\delta \sim 80°$, respectively. Fault $B$ has fault strike azimuth and fault dip angles $\phi \sim 265°$ and $\delta \sim 82°$, respectively.
These faults can be seen as small steps of less than 30 metres in the horizon between the late Carboniferous underburden and the Rotliegend reservoir. The reservoir thickness around the Huizinge tremor hypocentre hardly varies.

The elastodynamic rock properties of the subsurface formations around the tremor epicentre have been calculated from the rock density $\rho$ [kg/m$^3$] and the primary (P) and secondary (S) wave velocities $V_p$ and $V_s$ [m/s]. They originate from NAM's seismic velocity model which has been updated in 2015 and was also used in Wentinck (2017)[2]. Table A.1 in Appendix A shows the names and mean depths of the formations for which the rock density and wave velocities have been defined by this velocity model.

The observed displacements are from the recordings of the Middelstum, Westeremden, Stedum, Kantens, Garsthuizen and Winneweer ground accelerometers operated by KNMI. The station locations are listed in Appendix A, Table A.4 . The observed displacements are shown in Chapter 3.

[1]The fault strike azimuth angle is the angle between the Earth north direction and the fault strike where it is measured clockwise round from north.

[2]The NAM model has been provided by Remco Romijn from NAM in the form of Excel and .csv files.

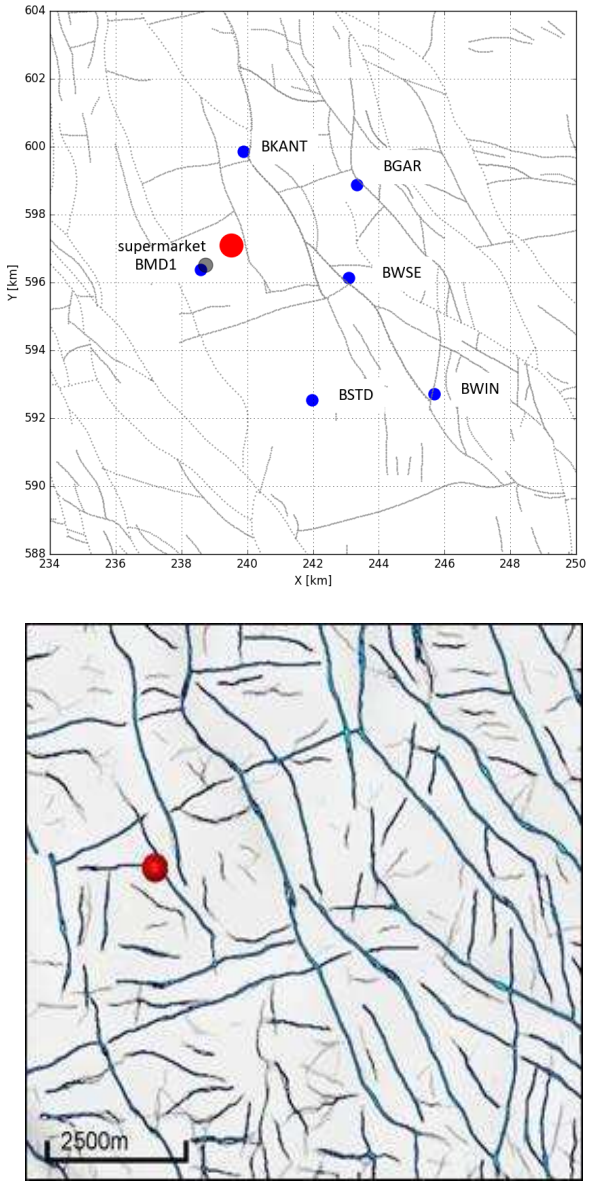


Figure 2.1 : Top figure: Faults and locations of preferred tremor epicentre (red dot) and the Middelstum, Westeremden, Stedum, Kantens, Garsthuizen and Winneweer ground accelerometers (blue dots) in the region around the Huizinge tremor in Dutch Rijksdriehoeksstelsel (RD) coordinates. The black dot shows the location of a supermarket in Middelstum which recorded ground motions with a camera, see discussion. The faults shown are from a NAM database that includes the fault dip, throw and azimuth angles. The thin grey dotted and solid fault lines shown are intersections of the faults with the top horizon of the Rotliegend reservoir. The preferred epicentre location of the tremor is from Dost and Kraaijpoel (2013). The RD coordinates of the tremor epicentre and ground accelerometers are given in Appendix A, Table A.4 .

Bottom figure: Faults and location of preferred tremor epicentre (red dot) recently found by Kortekaas and Jaarsma (2017) from EBN using fault plane tracking algorithms (or ant-tracking) on seismic data.
Fault $A$ through the tremor hypocentre is in NNW-SSE direction with the foot wall on the west side. Fault $B$ through the tremor hypocentre is in W-E direction with the foot wall on the north side.

# Chapter 3

# Set up of finite element method simulations

The model uses realistic profiles for the wave velocities in the deep subsurface formations above the reservoir. Two subsurface domains of several kilometres around the tremor hypocentre have been used for the simulations. The first domain is the same as the one used for the first series of simulations, see the aforementioned report. Since the location of the Winneweer ground accelerometer was outside the boundaries of this domain, a second, larger subsurface domain has been made which includes this location.
In addition, the subsurface horizons of the formations in this domain have been more accurately triangulated by importing them in the form of so-called .STL type files. Also, the horizons explicitly include those of the floater and anhydrite layers in the Zechstein formation. The lowest horizon of the domain is the base of the late Carboniferous[1]. These small differences between both domains do not lead to significant different displacements.

According to Dost et al. (2018), the moment magnitude $M$ [Richter] is about equal to the local magnitude $M_L$ [Richter][2]. Using $M_L = M \sim 3.4$ and Kanamori's relation between

[1] Although the lowest horizon was modelled as a reflecting boundary, downwards propagating waves reflected at this interface did not interfere with the direct body waves for the time intervals of interest.

[2] The determination of the moment magnitude $M$ from the measured local magnitude $M_L$ by stations around the tremor epicentre has been improved for the tremors in the Groningen field in the last 6 years but may be confusing for the reader. According to Dost and Kraaijpoel (2013), an average of the 8 most reliable borehole data within a hypocentre distance of 50 km give a value for the Huizinge tremor $M_L$ 3.4 $\pm$ 0.1. The corresponding seismic moment derived from the subsurface model used at that time was estimated $M = 3.6 \pm 0.1$, with the remark that this derivation was subject to further investigation. Contrarily, the following models indicated that the moment magnitude $M$ was on average 0.2 units smaller than the local magnitude $M_L$, see Dost et al. (2016). Recently, the latest correlations from Dost et al. (2018), indicate $M \sim M_L$ for tremors $M > 2.5$.
In Wentinck (2017), we have used for the simulated tremor $M = 3.55$. Unfortunately, the introduction of this report incorrectly states that the tremor has a local magnitude $M_L = 3.6$ instead of stating that it has a moment magnitude $M = 3.6$. Following Dost et al. (2016), we have subtracted 0.2 units and have added 0.15 units to this value, resulting in a moment magnitude $M = 3.55$. The addition accounts for the amplification of S waves in the shallow subsurface. Further, we divided the amplitude of the vertical

seismic moment $M_0$ [J] and moment magnitude $M$, i.e., $\log M_0 = 3/2(M + 6.07)$, the corresponding seismic moment $M_0$ of the simulated tremor is $M_0 = 160$ TJ.

The following subsurface formations have been considerably simplified considering that this work is focussed on the low frequency content of the waves and that the ground accelerometers used are within a distance of 8 km from the tremor epicentre, see below. From top to bottom:

- The shallow subsurface, i.e., the sand, clay and peat layers within 100 m below the surface. Primarily, the shear modulus of these sediments is small compared to the one of the deeper rock. It leads to a significantly lower S wave velocity and a relatively strong attenuation of S waves in the shallow subsurface. The combined effect is a ground motion amplification of the S waves of about a factor 2, in agreement with Dost et al. (2004), a delay of the S wave arrivals at the ground accelerometers of about 0.2 - 0.3 s and some bending of the S wave vertically upwards. This amplification adds to the usual amplification of subsurface waves when reaching the free surface[3].
  In the simulations, we do not include an explicit detailed velocity model for the slow down of the S wave in the shallow subsurface. Since the S wave primarily manifests itself in the radial and transverse components of the displacements, we multiply the simulated horizontal components with a factor 2 to account for the amplification of the S wave in the shallow subsurface. The P wave, which manifests itself primarily in the vertical component, hardly slows down in the shallow subsurface and is not amplified. We assume that the vertical ground displacements during the passage of the P wave are in this respect quite well modelled.

- The Brussel Sandstone member in the lower North Sea formation is disregarded. Incorporating this relatively hard sandstone would lead to lower travel times through the North Sea formation than would follow from the velocity model used and would lead to some scattering of high frequency waves passing through it[4]. The thickness of this layer is less than 200 m. It is poorly mapped and it is believed that it could substantially vary over the field.

- The Triassic, Altena and Rijnland formations have been grouped to form a single subsurface formation. The P and S velocities in this formation are weighted means

displacement by a factor 2 because the vertical component predominantly shows the P wave and this wave is hardly or not amplified in the shallow subsurface.
In the present report, using $M_L = 3.4$, we amplify the horizontal signals by a factor two to include the amplification of the S wave in the shallow subsurface and don't divide the amplitude of the vertical displacement to keep it simple. This leads to practically the same results as in the first report.

[3]In the FEM simulations, the amplification of waves reaching the surface is automatically calculated using the appropriate boundary condition at the surface.

[4]According to check shots with explosives in the field significantly lower travel times to the surface are observed than modelled for direct P waves between 4 - 7 km from the epicentre, see Langemeijer (2017), Figure 28. The author suggests that this may be due to presence of this sandstone.

of the velocities in these three formations[5].

- The floater and anhydrite layers which are part of the Zechstein salt above the reservoir have a constant thickness to solve meshing problems.
- The late Carboniferous and the formations below the late Carboniferous are assumed to be uniform over the region of interest. The velocity profile as a function of depth in these formations is assumed to be typical and wave reflections from below the base of the reservoir are ignored[6].

Two FEM simulations have been done for each fault identified by EBN. One simulation is for slip along fault dip with a rake angle of -90°. The other is for slip along fault strike with a rake angle of 0°. Ground displacements for other slip directions follow from adding weighted displacements from these two simulations, using the superposition principle for linear processes, such as elastic wave propagation.

In general, a seismic source can be modelled as a point source or as an extended source. For a point source, the dimensions of the slip plane and the rupture velocity[7] are indistinguishably included in the time dependence of the so-called source time function. For a point source, this function completely defines the dynamics of the rupture process or the relaxation of elastic forces on the slip plane over time. For an extended source, the rupture velocity and the dimensions of the slip plane are both explicitly included in the

[5]The weighting ensures that the travel times of vertical P and S waves in the combined formation are equal to the travel times of these waves through the three stacked formations.

[6]The pre- or sub-Permian formations below the reservoir are not uniform over the Groningen field. During the Namurian period in the late Carboniferous, mainly basin facies, such as shales, mudstones and peat, were deposited in the Groningen area. During the later Westphalian period in the late Carboniferous, a deltaic river system progrades from the south-east depositing more sandy sediments and non-uniformly filling valleys in a fluvial area. These sediments directly subcrop the Rotliegend sandstone in the Groningen field. According to the so-called Dutch Velmod-2 project, the P wave velocity in the top of the Namurian gradually varies over the Groningen field, see for example Langemeijer (2017), Figure 22 for the north-east Netherlands.
Significant wave reflections can be expected from the horizon between the Dinantium and Namurian (or between the early and late Carboniferous) formations at more than 6 km depth in the Huizinge area. Such waves travel at least 6 km through the Namurian formation before they pass again the horizon between the late Carboniferous and Rotliegend formations while moving upwards. For typical mean P and S wave velocities in the Namurian of about 5 and 3 km/s, the reflected P and S waves arrive at the surface at least 1.2 and 2 s after the corresponding direct body waves in the area of interest.
Also, the late Devonian carbonates and early Carboniferous (or Dinantium, Mississippian or Visean) carbonate limestones at varying depth over the field but deep below the reservoir guide and redirect downwards propagating (or diving) waves back to the surface because waves in these rocks have propagate faster than in the overlying late Carboniferous (Pennsylvanian) siliclastics (or sandstones/shales). According to one-dimensional ray tracing models and two-dimensional full wave propagation finite difference models, such waves appear first at the surface at a distance of more than 10 km away from the epicentre, see for example Spetzler and Dost (2017) and Langemeijer (2017). For the Huizinge tremor and the stations of interest, these so-called diving waves hardly interfere with the direct body waves when reaching the surface.

[7]The rupture velocity is the velocity with which the rupture front propagates over the slip plane.

seismic source model.

In this work, the rupture plane of the seismic source has been divided in a number of relatively small slip patches along fault strike. For each slip patch, two double couples and a source time function are defined. The source time function describes how the double couple forces develop over time. They are the same for each slip patch except for a time shift which is determined by the rupture velocity and the location of the slip patch with respect to the hypocentre of the tremor. The extended seismic source is the same as the one used in Wentinck (2017), see this reference for details. For convenience, the main features of the source time functions are given in Appendix B.

# Chapter 4

# Results

Lacking an absolute time line for the observations with respect to the start of the rupture and herewith uncertainty about the depth of the tremor hypocentre, and considering the simplifications in the subsurface velocity model and the numerical errors following from the mesh of the subsurface model[1], we can only partly reconstruct the seismic source from a few prominent features in the observed and simulated displacements.

In the following, we firstly determine which fault, as identified by EBN, slipped most likely and we determine the slip direction. Secondly, we say more about the multiple oscillations (multiples) in the ground displacements during the passage of the S wave as observed by a few ground accelerometers.

Without an absolute time line for the observed signals, we have shifted the time axis of the observed displacements such that the arrivals of the P wave optimally coincide with the simulated ones. This implies that the observed and simulated peaks of the S wave, in general, do not coincide. One reason is that the latter are in reality somewhat delayed by slow shear wave propagation in the shallow subsurface. This delay, which is not included in the simulations, can be in the range 0.2 - 0.3 seconds. Other reasons are that the tremor hypocentre depth may be not correct or the velocity model for the North Sea formation does not properly include the Brussel Sandstone member herein.

## 4.1 Reconstruction of horizontal accelerometer orientations from maximising the magnitude of the radial component of the P-wave

One method to reconstruct the orientations of the ground accelerometers is by rotating them in the horizontal plane to obtain a maximal mean rms value of the radial component

[1]The mesh size chosen determines the bandwidth of the simulated signals and sometimes leads to artificial oscillations at frequencies above a few Hertz.

of the accelerations $|a_{rad}|$ [m/s$^2$] during the passage of the P wave[2]. Following the usual conventions, the radial component is parallel to the line connecting the locations of the tremor epicentre and the receiver and in the direction of the receiver. The transverse component is perpendicular to this line and in the direction of the right hand with the face towards the receiver. The vertical component is positive in upwards direction.
The idea behind this method is that the compressive P wave can be primarily decomposed in a vertical and in a radial component when it reaches the surface, especially in the far field. The method requires to define a time window in which the P wave passes the accelerometers. Usually, the first part of the vertical signal indicates this somewhat arbitrarily chosen time window. For weak signals, and especially for the ground accelerometers, care must be taken to eliminate artificial (low frequency) displacements following from electronic disturbances in the sensors and signal amplifiers. KNMI has performed this task, providing the displacement components for all ground accelerometers.

Using the reconstructed orientations, KNMI obtained the so-called the fault strike azimuth and fault dip angles and slip direction (the so-called focal sphere of the tremor) from the computer programme Focmec[3]. According to this program, the fault plane has fault strike azimuth and fault dip angles $\phi \sim 320^\circ$ and $\delta \sim 80^\circ$, respectively. These parameters have been used in Wentinck (2017).
Figures A.6 and A.7 in Appendix A show $|a_{rad}|$ during the passage of the P wave for all ground accelerometers as a function of the horizontal orientation of the accelerometers. Indeed, $|a_{rad}|$ is satisfactorily maximal for the reconstructed accelerometer orientations.

Signals from several recent tremors, which have been recorded by the expanded and calibrated geophone/ground accelerometer network in the Groningen field, show that the radial component of downhole geophones at 200 to 50 m depth have indeed a maximal value for $|a_{rad}|$. However, for the ground accelerometers, $|a_{rad}|$ frequently and substantially deviates from a maximal value during the passage of the P wave, see Appendix A, §A.3. Hence, we doubt whether the reconstruction of the orientations of the ground accelerometers by this method is robust and we have tried another method to determine the seismic source parameters.

[2]Consequently, the corresponding rms value of the transverse component $|a_{tra}|$ values is minimal.

[3]This programme performs a systematic search of the focal sphere and reports acceptable solutions based on selection criteria for the number of polarity errors and errors in amplitude ratios. The input are the polarities (P, SV, SH) and/or amplitude ratios (SV/P, SH/P, SV/SH). P, SV and SH are measures of the strength of the displacements during the passage of the P and S waves, in the propagating, vertical and transverse directions of the wave.

## 4.2 Method based on vertical displacements and on the magnitude of horizontal displacements

Since both the vertical displacement and the magnitude of the horizontal observed displacements do not depend on the horizontal orientations of the ground accelerometers, we firstly evaluate how these displacements compare with the simulated displacements for the two faults $A$ and $B$ for various slip directions or rake angle $\lambda$. Hereafter, we rotate the ground accelerometers in the horizontal plane to obtain the best match between the observed and simulated radial and transverse S wave components.

Figures 4.1 and 4.2 show the results. The observed displacements have been filtered using a 0.3 Hz high-pass regression filter in addition to the first order 0.1 Hz high-pass filter of the accelerometer data-logger system. The simulated displacements have been filtered similarly.

The green and black lines in Figures 4.1 and 4.2 show the vertical and total horizontal displacements which are invariant under rotation of the ground accelerometer. The red and blue lines show the radial and transverse components after rotation of the ground accelerometers, see Appendix A, §A.2 for the rotation angles used.

Comparing the observed and simulated signals for all stations, it seems that fault $A$ ruptured with a slip direction of the hanging wall predominantly downwards. The slip on fault $B$ would have been more along fault strike. It reproduces less well the displacements of the Westeremden and Garsthuizen stations. In addition, the simulated time interval between the passages of the P and S waves, $\Delta t_{PS}$ [s] for slip along fault $A$ corresponds better with the observed one for the Winneweer station. The simulated strong negative vertical ground motion during the arrival of the P wave is not observed for the same, expected time difference between the passages of the P and S waves, $\Delta t_{PS}$. According to these comparisons, it seems that slip along fault $A$ is more likely than slip along fault $B$ although simulations of slip along fault $B$ somewhat better reproduce the observed displacements of the Stedum station.

In Appendix A, §A.4, the observed time difference of the observed and simulated arrival times of the P and S waves $\Delta t_{PS}$ [s] are plotted against the distance of the stations from the tremor epicentre. The simulated arrival times of the P and S waves fairly well correspond with ray tracing calculations for a point source using 5 subsurface layers.

## 4.3 Multiple oscillations

During the passage of the P wave, the vertical displacements of the Middelstum, Westeremden, Kantens and Stedum stations oscillate twice. The time period of the oscillations is about 0.6 s. These oscillations are not or hardly reproduced by the simulations except

for the Stedum ground accelerometer for slip along fault $B$.

During the passage of the S wave, the total horizontal displacements of the Middelstum and Westeremden stations oscillate three and two times with less or about equal strength, respectively. For the Kantens station, 3 oscillations of diminishing strength are observed. Multiple oscillations are less clear if at all for the Garsthuizen, Stedum and Winnerweer stations. The simulations don't support the observed strong oscillations of the Middelstum and Westeremden stations.

All kind of combinations of slip or seismic events on both fault $A$ and fault $B$ with some time delay between the start of them do not lead to a better correspondence between simulated and observed displacements. Such combinations have been done under the restriction that a specific accelerometer orientation should be the same for subsequent slip events.

Investigations of recent tremors in the Groningen field indicate that these fundamental discrepancies between observed and simulated displacements likely originate from wave scattering in the shallow subsurface. Appendix A, §A.3 shows examples of similar oscillations in the ground motions of the ground accelerometers which are not observed in the motions of the geophones in the shallow boreholes at 50 - 200 m depth.

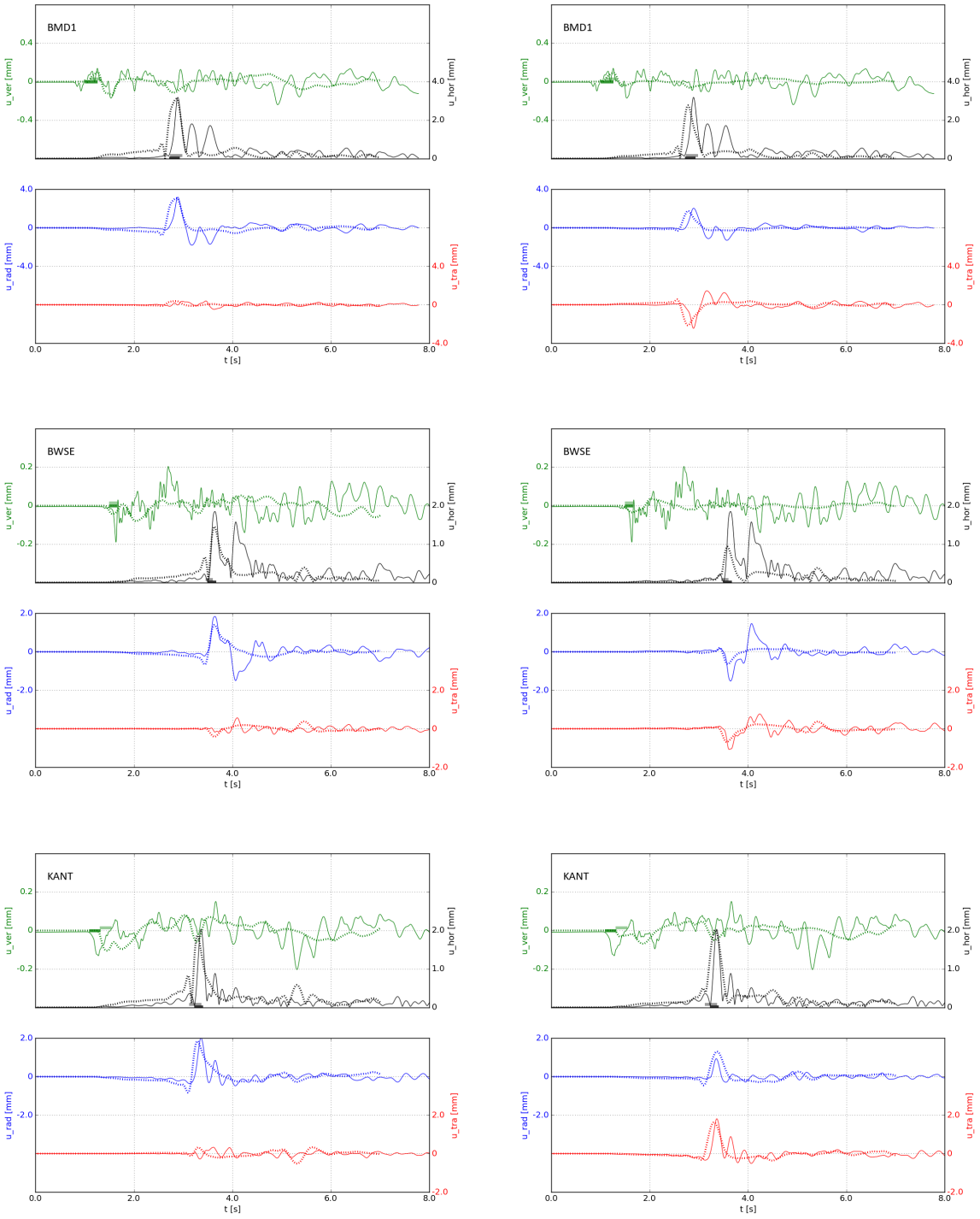


Figure 4.1 : Observed (solid) and simulated (dashed) vertical (green) and horizontal (black) displacements following from the Huizinge 2012 tremor.
The left and right figures are for slip on fault $A$ with a rake angle $\lambda$ = -90° and on fault $B$ with a rake angle $\lambda$ = -150°, respectively.

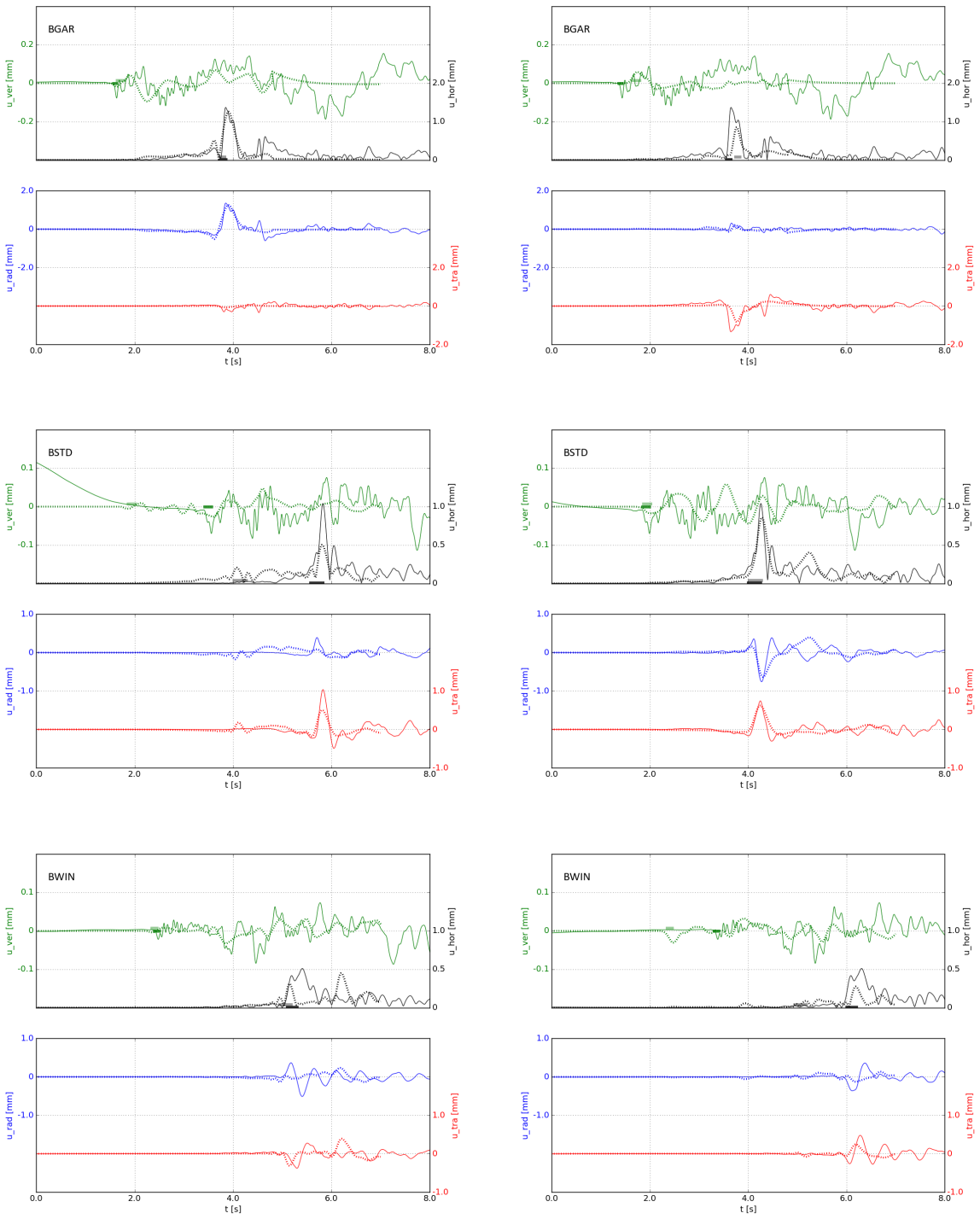


Figure 4.2 : Observed (solid) and simulated (dashed) vertical (green) and horizontal (black) displacements following from the Huizinge 2012 tremor.
The left and right figures are for slip on fault $A$ with a rake angle $\lambda$ = -90° and on fault $B$ with a rake angle $\lambda$ = -150°, respectively.

# Chapter 5

# Discussion

From the present work, we conclude that the reconstruction of the ground accelerometer orientations from a maximal radial energy during the passage of the P wave is not robust. While practically all displacements of downhole geophones at 50 - 200 m depth in shallow boreholes show indeed a maximal radial energy during the passage of the P wave, there are frequently remarkable deviations from this behaviour for the displacements of the ground accelerometers.

Without a robust method to reconstruct the orientation of the ground accelerometers which recorded the Huizinge tremor, we have used another method to derive the seismic source parameters. This method uses that the vertical displacement and the magnitude of the horizontal displacements do not change when the ground accelerometers are rotated in the horizontal plane. Furthermore, we have assumed that the slip plane coincides with one of the two faults that have been identified by EBN at the tremor epicentre from ant-tracking and that the tremor hypocentre is located in the reservoir at 3 km depth.

Under these assumptions the ground displacements from simulations have been compared with the observed ones for both faults by varying the slip direction as the remaining unknown seismic source parameter for all six ground accelerometers near the tremor epicentre. Likely, the fault that slipped is fault $A$ in NNW - SSE direction and where the hanging wall predominantly slipped downwards. This conclusion is primarily based on the comparison of the simulated and observed signals of the Westeremden, Garsthuizen and Winneweer stations.
The conclusion is consistent with ground motions which have been recorded by a security camera in a supermarket in Middelstum[1]. The camera looks into the gangway between the shelves with products which is more or less in north-south direction. Bottles and other products in the shelves move almost perpendicular to the gangway, due to the S wave in radial direction.

[1]This movie is available on YouTube under the name "Eerste beelden van aardbeving Leermens verschenen - RTV Noord".

The multiple, or second observed peak in the displacements, during the passage of the S wave, such as for the Middelstum station, is not observed at all stations. According to KNMI, it is also not observed by a geophone in a borehole more than 10 kilometres away from the Huizinge tremor epicentre[2]. A second slip event during the generation of the tremor is not likely. The kinematic modelling done so far, indicates that the second peak does not follow from reflections of seismic waves in the deep subsurface. Possibly, the second peak is a multiple which follows from S wave reflections in the shallow subsurface. Recent tremors in the Groningen field show that in several cases, significant similar low-frequency multiples are observed by the ground accelerometers but not by the downhole geophones below them.

The original goal of this work was to determine the dimensions of the slip plane from a detailed analysis of the ground motions. This goal is not achieved with the present work. Although the extended seismic source used fairly well reproduces the shape of the main displacement during the passage of the S wave for several stations, there are also significant discrepancies, such as for the Winnerweer and Middelstum stations.
It could well be that another extended source would give a better match with the observed signals. It remains a major task to find one regarding the uncertainty in the orientations of the ground accelerometers. Also, it requires a calibrated model for wave propagation and wave scattering in the shallow subsurface in the region around the epicentre of the Huizinge tremor.

[2]Signals of this geophone are much harder to use because of interference between direct body waves and diving waves which return to the surface.

# Chapter 6

# Acknowledgements

I thank Remco Romijn and Clemens Visser (NAM) for providing me the field data and the velocity model, Marloes Kortekaas (EBN) for providing me the faults from ant-tracking near the Huizinge tremor epicentre and Bernard Dost (KNMI) for providing me the accelerometer data and a plausible fault orientation and slip direction. I thank all and Steve Oates (SGS-I) for reviewing this report and Xander Campman and Ewoud van Dedem (SGS-I) for other comments and suggestions.

# Bibliography


Aki, K., and Richards, P. G., "Quantitative Seismology", University Science Books, 2009.

Bommer, J. J., Dost, B., Edwards, B., Rodriguez-Marek, A., Kruiver, P., Meijers, P., Ntinalexis, M., and Stafford, P. J., "Development of Version 2 GMPEs for Response Spectral Accelerations and Significant Durations from Induced Earthquakes in the Groningen Field",, Technical report, Nederlandse Aardolie Maatschappij B.V., the Netherlands, 2015.

Bommer, J. J., "Overview of Development of Current Ground-Motion Model for the Groningen Field",, Technical Report presentation for Groningen GMPE Workshop, London, 18-20 July 2016, Independent consultants to NAM, 2016.

Burnett, W., "3D Finite Difference Wavefield Modeling for Ground Motions",, Technical Report presentation for Groningen GMPE Workshop, London, 18-20 July 2016, ExxonMobil URC, Houston, 2016.

Dost, B., and Haak, P. J., "A Comprehensive Description of the KNMI Seismological Instrumentation",, Technical Report Technical report TR-2452002, Koninklijk Nederlands Metereologisch Instituut, the Netherlands, 2002.

Dost, B., and Kraaijpoel, D., "The August 16, 2012 Earthquake near Huizinge (Groningen)",, Technical Report KNMI report TR 16/1/2013, Koninklijke Nederlands Meteorologisch Instituut, the Netherlands, 2013.

Dost, B., van Eck, T., and Haak, H., "Scaling of Peak Ground Acceleration and Peak Ground Velocity Recorded in the Netherlands", Bollettino di Geofisica Teorica ed Applicata, 45, 153–168, 2004.

Dost, B., Edwards, B., and Bommer, J. J., "Local and Moment Magnitudes in the Groningen field",, Technical Report unpublished report, 4 March 2016, Koninklijke Nederlands Metereologisch Instituut, Netherlands, 2016.

Dost, B., Edwards, B., and Bommer, J. J., "The Relationship between $M$ and $M_L$: A Review and Application to Induced Seismicity in the Groningen Gas Field, The Netherlands", Seism. Res. Letters, 89, 1062–1074, 2018.

Dost, B., "Moment Tensor Solutions for Groningen Earthquakes",, Technical Report presentation for Groningen GMPE Workshop, London, 18-20 July 2016, Koninklijke Nederlands Metereologisch Instituut, the Netherlands, 2016.

Edwards, B., Bommer, J., Stafford, P., and Rodrigues-Marek, A., "Inversion of Ground Motions for Source, Path and Site Parameters and Generation of Stochastic Records",, Technical Report presentation for Groningen GMPE Workshop, London, 18-20 July 2016, Independent consultants to NAM, 2016.

Graves, R. W., and Pitarka, A., "Broadband Ground-Motion Simulation using a Hybrid Approach", Bull. Seis. Soc. Am., 100, 2095–2133, 2010.

Graves, R. W., and Pitarka, A., "Refinements to the Graves and Pitarka (2010) Broadband Ground-Motion Simulation Method", Seismological Research Letters, 86, 1–6, 2015.

Kortekaas, M., and Jaarsma, B., "Improved Definition of Faults in the Groningen Field using Seismic Attributes", submitted to Netherlands Journal of Geosciences, -, –, 2017.

Kraaijpoel, D., and Dost, B., "Implications of Salt-related Propagation and Mode Conversion Effects on the Analysis of Induceed Seismicity", Journal of Seismology, 17, 95–107, 2013.

Langemeijer, J., "Estimation of an Effective Velocity Model for the pre-Permian below the Northeast Netherlands",, Technical Report Master thesis, September 2017, University Utrecht, EBN, KNMI, the Netherlands, 2017.

Lawrence, Z., Gans, C., Bailey, J., Burnett, W., Gist, G., and Reilly, J., "Groningen Seismic Observations and Independent Event QC",, Technical Report presentation for NAM/URC Groningen Workshop, 4-6 March 2015, ExxonMobil URC, Houston, 2015.

NAM, "Geological Schematisation of the Shallow subsurface of Groningen for Site Response to Earthquakes for the Groningen gas field, Deltares report",, Technical report, Nederlands Aardolie Maatschappij B.V., the Netherlands, 2015.

Scholz, C. H., "The Mechanics of Earthquakes and Faulting, $2^{nd}$ edition", Cambridge University Press, 2002.

Spetzler, J., and Dost, B., "Hypocentre Estimation of Induced Earthquakes in Groningen", Geophys. J. Int., 209, 453–465, 2017.

Stafleu, J., Gunnink, J., de Lange, G., and Kruiver, P., "Shear Wave Velocity for the Upper 30 m - Combining the GeoTOP 3D Voxel Model and Seismic CPT's",, Technical Report presentation for workshop SoDM, 17 march 2016, TNO, Utrecht, Houston, 2016.

Stein, S., and Wysession, M., "An Introduction to Seismology, Earthquakes, and Earth Structure", Blackwell Publishing, 2003.

Terrell, M., "Structural Overview and Max Magnitude Summary",, Technical Report presentation for Groningen GMPE Workshop, London, 18-20 July 2016, ExxonMobil URC, Houston, 2016.

Udias, A., Madariaga, R., and Buforn, E., "Source Mechanisms of Earthquakes - Theory and Practice", Cambridge University Press, 2014.

van Dedem, E. J., "Ground Motion Modeling for Groningen",, Technical Report presentation for Groningen GMPE Workshop, London, 18-20 July 2016, Shell Global Solutions International, Rijswijk, 2016.

Wentinck, H. M., "Kinematic Modelling of Large Tremors in the Groningen Field using Extended Seismic Sources - First Results related to the Huizinge 2012 Tremor",, Technical Report report for NAM, Shell Global Solutions International B.V., 2017.

Zhu, L., and Ben-Zion, Y., "Parametrization of General Seismic Potency and Moment Tensors for Source Inversion of Seismic Waveform Data", Geophys. J. Int., 194, 839843, 2013.

# Appendix A

# Field data and ground accelerometer data

## Appendix A.1 field data and tremor and ground accelerometer coordinates

Table A.1 shows the names of the subsurface formations used in the seismic velocity model 2015 and the mean, maximal and minimal depths of the lower horizons of these formations in the region around Huizinge. Table A.2 shows the rock types in these formations. Table A.3 shows the parameters used for the velocity model. Figure A.1 shows the P and S wave velocity profiles used.

Table A.4 shows the Dutch Rijksdriehoeksstelsel (RD) coordinates of the location of the epicentre of the Huizinge tremor, the ground accelerometers of interest and the distance between them and the tremor epicentre[1].

[1]The RD coordinates are derived from latitude and longitude data provided by KNMI, using the application "GPScoordinaten" at www.gpscoordinaten.nl.

Table A.1 : Mean depths of the lower horizon (or the base) of the formations around the Huizinge tremor epicentre which are used in the seismic velocity model of NAM, update 2015 in a 10×10 km area around the Huizinge tremor and defined by the following RD coordinates: $X_{min} = 235$ km, $X_{max} = 245$ km and $Y_{min} = 590$ km, $Y_{max} = 600$ km. Further, the table shows the mean thickness of these formations and the standard deviation, minimum and maximum values of the depths of the lower horizons. The minimum and maximum values are averages in square grid cells of 500×500 m.

| Formation name used | mean depth lower horizon m | mean thickness m | stdev lower horizon m | min. value lower horizon m | max. value lower horizon m |
|---|---|---|---|---|---|
| Upper North Sea | -350 | 350 | 26 | -495 | -315 |
| Lower North Sea | -850 | 500 | 44 | -961 | -764 |
| Chalk | -1690 | 840 | 56 | -1837 | -1509 |
| Rijnland | -1775 | 85 | 57 | -1930 | -1571 |
| Altena | - | - | - | - | - |
| Triassic | -1935 | 60 | 103 | -2199 | -1765 |
| Upper Zechstein | -2178 | 143 | 154 | -2526 | -1781 |
| floater | -2225 | 47 | 164 | -2633 | -1815 |
| Lower Zechstein | -2825 | 600 | 98 | -3178 | -2706 |
| anhydrite | -2876 | 51 | 98 | -3230 | -2750 |
| Rotliegend reservoir | -3144 | 268 | 104 | -3506 | -3002 |
| Carboniferous underburden | < -6000 | | | | |

Table A.2 : Rock type of the formations in the seismic velocity model 2015 of NAM.

| formation name | rock type |
|---|---|
| Upper North Sea | Quarternary shallow marine to terrestial clay and fine to course sands |
| Lower North Sea | Tertiary shallow marine clays, sands and sandstones |
| Chalk | Cretaceous shallow to deep-marine limestone |
| Rijnland | Cretaceous shallow marine marlstone, claystone and interbedded sandstones |
| Altena | Jurassic marine claystone |
| Triassic | Triassic lower Bundsandstein formation: lacustrine claystone, siltstone and very fine sandstone |
| upper Zechstein | Zechstein evaporite, rock salt |
| floater | Zechstein floater, anhydrite |
| lower Zechstein | Zechstein evaporite, rock salt |
| anhydrite | Anhydrite and dolomite |
| Rotliegend reservoir | Ten Boer claystone - lacustrine shale with thin sandstone<br>Slochteren sandstone reservoir - mixed fluvial-aeolian sandstone |
| Late Carboniferous underburden | lacustrine and floodplain siltstones, organic shales and lower delta plain fine sandstones |

Table A.3 : Input parameters for the velocity model 2015 of NAM for the various subsurface formations and used in the FEM simulations.

| formation name | $V_{p,0}$ m/s | $k_p$ 1/s | $V_{s,0}$ m/s | $k_s$ 1/s |
|---|---|---|---|---|
| Upper North Sea | 1733 | 0.500 | 458 | 0.430 |
| Lower North Sea | 1922 | 0.500 | 614 | 0.430 |
| Chalk | 680 | 2.300 | -5 | 1.390 |
| Rijnland | 2125 | 0.500 | 701 | 0.420 |
| Altena | 2222 | 0.355 | 1364 | 0.190 |
| Triassic | 2383 | 0.680 | 1450 | 0.380 |
| upper Zechstein | 4300 | 0 | 2436 | 0 |
| floater | 5729 | 0 | 3152 | 0 |
| lower Zechstein | 4475 | 0 | 2524 | 0 |
| anhydrite | 6000 | 0 | 3288 | 0 |
| Rotliegend reservoir | 3800 | 0 | 2232 | 0 |
| Carboniferous underburden | 2572 | 0.541 | 837 | 0.500 |

Table A.4 : The Dutch Rijksdriehoeksstelsel (RD) coordinates of the preferred epicentre of the Huizinge tremor and the KNMI ground accelerometers used. The last column shows the distance between the tremor epicentre and the ground accelerometers.

| name | abbreviation | ground accel. ser. no. | date | $M_L$ Richter | X m | Y m | dist. km |
|---|---|---|---|---|---|---|---|
| tremor | | | | | | | |
| Huizinge | | | 2012-08-16 | 3.4 | 239519 | 597095 | |
| KNMI stations | | | | | | | |
| Middelstum | BMD1 | 401 | | | 238581 | 596379 | 1.18 |
| Westeremden | BWSE | 834 | | | 243091 | 596144 | 3.70 |
| Stedum | BSTD | 117093 | | | 241973 | 592547 | 5.17 |
| Kantens | KANT | 115275 | | | 239881 | 599868 | 2.80 |
| Garsthuizen | BGAR | 115282 | | | 243327 | 598884 | 4.20 |
| Winneweer | BWIN | 115277 | | | 245681 | 592717 | 7.56 |

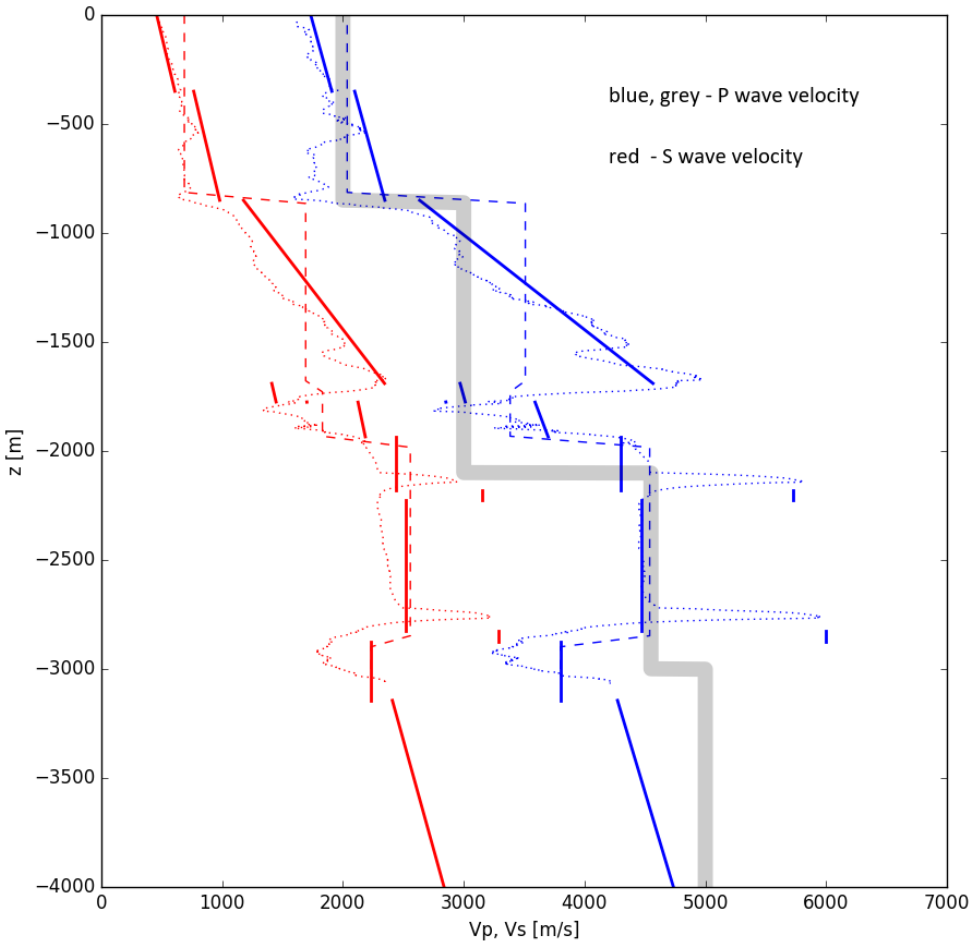


Figure A.1 : P and S wave velocity profiles. The solid line shows the wave velocities used in the FEM simulations. The dashed lines are the wave velocities used for calculating wave travel times with ray tracing, see §A.4. The thin dotted lines are the wave velocities measured in the Stedum observation well, within 5 km east from the tremor epicentre. For reference, the thick grey solid line shows the P wave velocity according to the 1D tremor hypocentre model from KNMI, which is an average model that is representative for the northern part of the Netherlands, see Spetzler and Dost (2017), Figure 7. In the Triassic, Altena, Rijnland and Chalk formations, the P wave velocity is substantially lower than the one we use for ray tracing.

# Appendix A.2 Ground accelerometer recordings

The ground accelerometers which recorded the Huizinge tremor are SIG AC-23 broadband accelerometers from GeoSIG$^{TM}$ (Switzerland) in combination with data loggers. They

have been part of the accelerometer surface network of the North Netherlands, operated by KNMI[2]. The main purpose of the accelerometers was to determine the tremor hypocentres and the peak ground accelerations. The polarity of the signals was in these years of less interest. In the following, we show the accelerations and velocities according to the latest processing by KNMI. The signals differ from those shown in Dost and Kraaijpoel (2013). From these signals we show below the displacements and accelerations the Fourier transforms of the displacements.

### A.2.1 Displacements and accelerations

Figures A.2 - A.5 show the vertical and horizontal and the radial and transverse displacements and accelerations of the ground accelerometers as provided by KNMI[3].
Figures A.6 and A.7 show the same data during the passage of the P-wave. In addition, they show the mean rms values of the amplitude of the radial accelerations $|a_{rad}|$ [m/s$^2$] during the passage of the P wave as a function of the horizontal rotation of the accelerometer. In satisfactorily agreement with the reconstruction of the orientation performed by KNMI, $|a_{rad}|$ obtains about maximal values for zero rotation for all stations. Deviations follow from the selected time window and signal filtering to suppress low-frequency electronic disturbances.

Figure A.8 shows the absolute values of the Fourier transforms (or frequency spectra) of the displacements. The spectra have a more or less flat low-frequency asymptote below 1 Hz and a high-frequency asymptote above 3 Hz which decays with $f^{-n}$ with $n \sim 3$ for the Middelstum and Kantens accelerometers. The decay is comparable with the high-frequency asymptote of the modified source time function we have used in the simulations but note that a possible effect of a frequency dependent wave attenuation in the subsurface has not been included yet[4].

[2]These 0.1 Hz - 100 Hz accelerometers have a temperature stability of 1 mV/°C at a full scale output of ± 10 V. The full scale corresponds to ± 0.1, 0.2, 0.5, 1, 2 and 4 g depending on jumper settings. The damping of the sensor is 'critical' with damping factor 0.7. The dynamic range is 125 dB. The sample frequency is 200 Hz. According to Dost and Haak (2002), §6, the bandwidth of the sensor is characterised by one pole (or first order) high-pass filter at 0.1 Hz and by a 2 pole (or second order) Bessel low-pass filter at 50 Hz. The signals have been sampled through a digital Hogenauer filter with a 3 dB point at 52 Hz. The result of these filters is a practically flat system response between 0.3 and 10 Hz and a steep fall off above 30 Hz, see Figure 6.2 in the aforementioned reference.
For accelerometers with 3 digit serial numbers, the sign of the vertical signal is positive in downwards direction. For accelerometers with 6 digit serial numbers, the sign of the vertical signal is positive in upwards direction, see Table A.4 . In this report the signs of the vertical signals have been converted. For all accelerometers the sign is positive when the displacement is in upwards direction.
After 2012, the SIG AC-23 accelerometers have been replaced by EpiSensor$^{TM}$ broadband DC - 200 Hz accelerometers from Kinemetrics, Inc., CA (US). For this reason, the orientation of the accelerometers in the horizontal plane cannot be checked anymore.

[3]The figures for the Middelstum, Westeremden and Kantens ground accelerometers have also been presented in Wentinck (2017) but for completeness, they are also shown in this report.

[4]The spectrum is a result of the rupture process dynamics and the frequency dependent wave attenuation in the subsurface. Further, it can be changed by the instrument response, data logging and signal

Table A.5 lists the rotations used to reconstruct the observed radial and transverse displacements when comparing them with the simulations for slip along fault A and for slip along fault B. These rotations differ.

Table A.5 : Clockwise rotations of the ground accelerometers to reconstruct the observed radial and transverse displacements to compare them with simulation results for slip along fault A and for slip along fault B.

| KNMI station | abbreviation | rotation for slip fault A degrees | rotation for slip fault B degrees |
|---|---|---|---|
| Middelstum | BMD1 | 0 | 50 |
| Westeremden | BWSE | 20 | 160 |
| Stedum | BSTD | 30 | -20 |
| Kantens | KANT | -20 | 270 |
| Garsthuizen | BGAR | 0 | 70 |
| Winneweer | BWIN | 45 | 160 |

processing. In this case, the fall-off for frequencies $< 0.3$ Hz is a result of the regression filter used by KNMI when processing the data. The high-frequency decay in the observed spectra is well below 30 Hz. Above 30 Hz, the response of the receiver system steeply falls off.

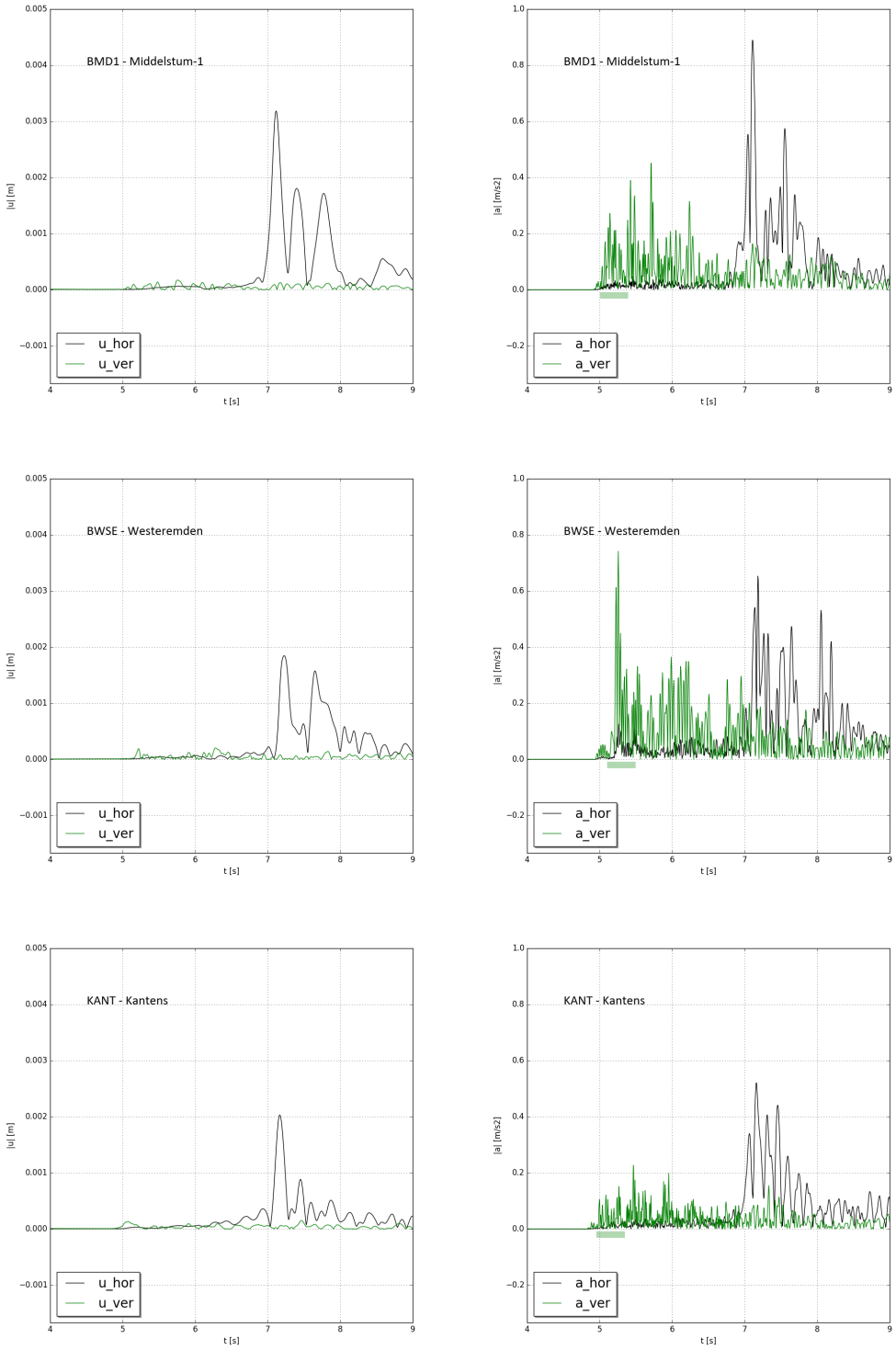


Figure A.2 : Displacements (left) and accelerations (right) of the Middelstum, Westeremden and Kantens accelerometers following from the Huizinge tremor.
The black and green curves show the magnitude of the horizontal and vertical displacements, $u_{hor}$ and $u_{ver}$ and corresponding accelerations $a_{hor}$ and $a_{ver}$, respectively. The green bar just below the time line defines the time window used to determine the energy of the horizontal components during the passage of the P wave.

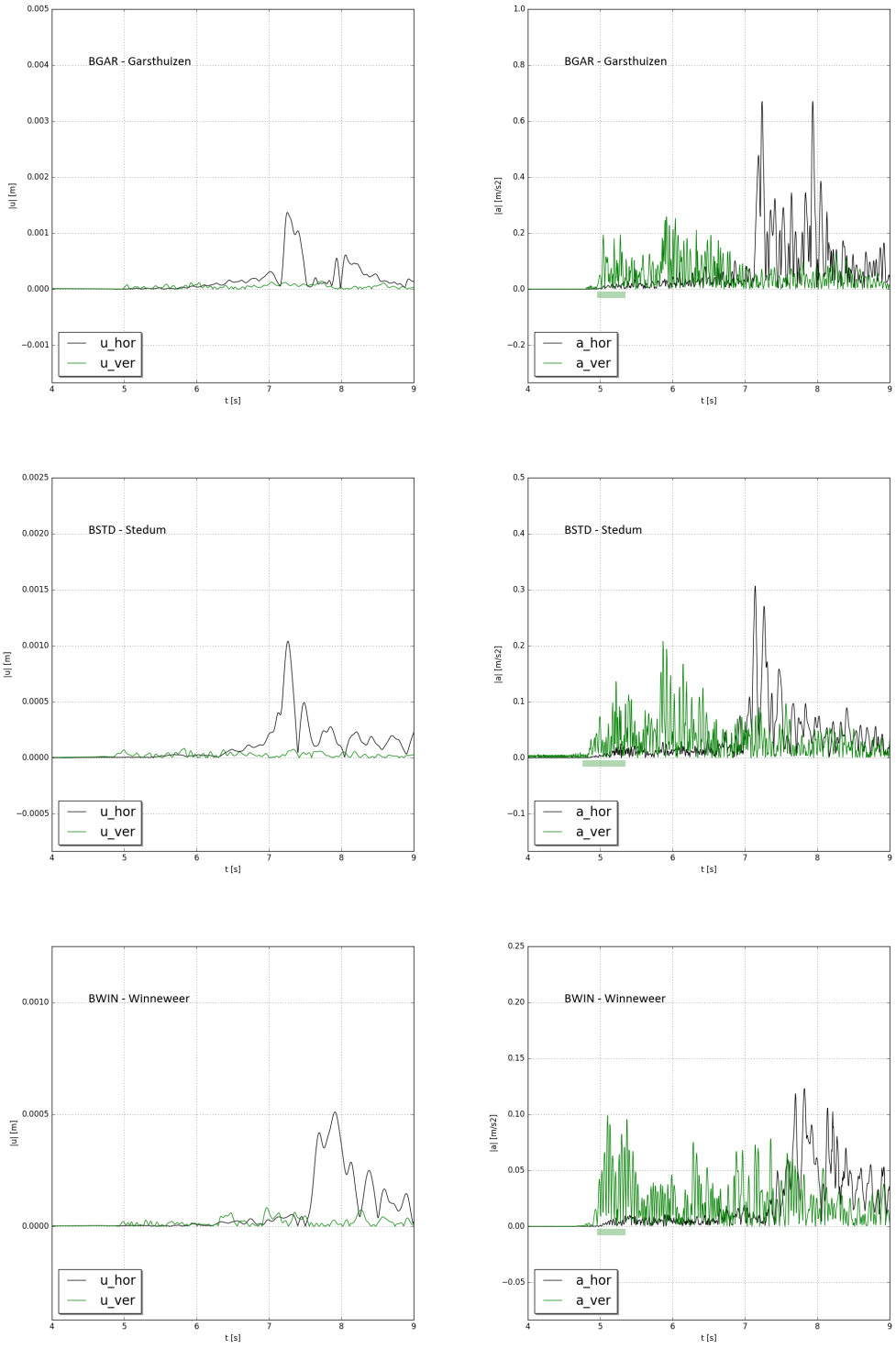


Figure A.3 : Displacements (left) and accelerations (right) of the Garsthuizen, Stedum and Winneweer accelerometers following from the Huizinge tremor.
The black and green curves show the magnitude of the horizontal and vertical displacements, $u_{hor}$ and $u_{ver}$ and corresponding accelerations $a_{hor}$ and $a_{ver}$, respectively. The green bar just below the time line defines the time window used to determine the energy of the horizontal components during the passage of the P wave.

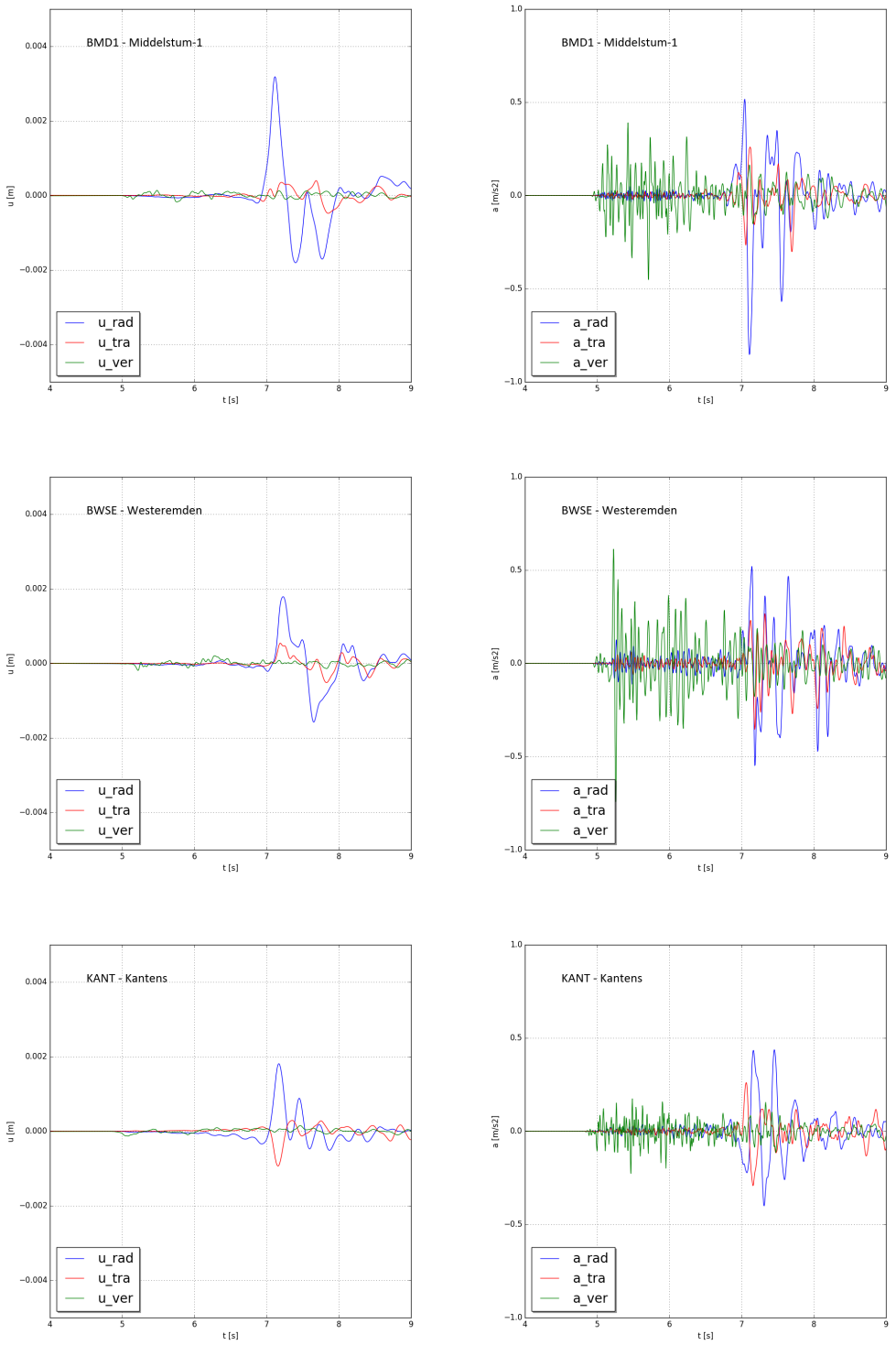


Figure A.4 : Displacements (left) and accelerations (right) of the Middelstum, Westeremden and Kantens accelerometers following from the Huizinge tremor. The signals originate from KNMI.
The blue, red and green curves show the radial, transverse and vertical displacements, $u_{rad}$, $u_{tra}$ and $u_{ver}$ and corresponding accelerations $a_{rad}$, $a_{tra}$ and $a_{ver}$, respectively.

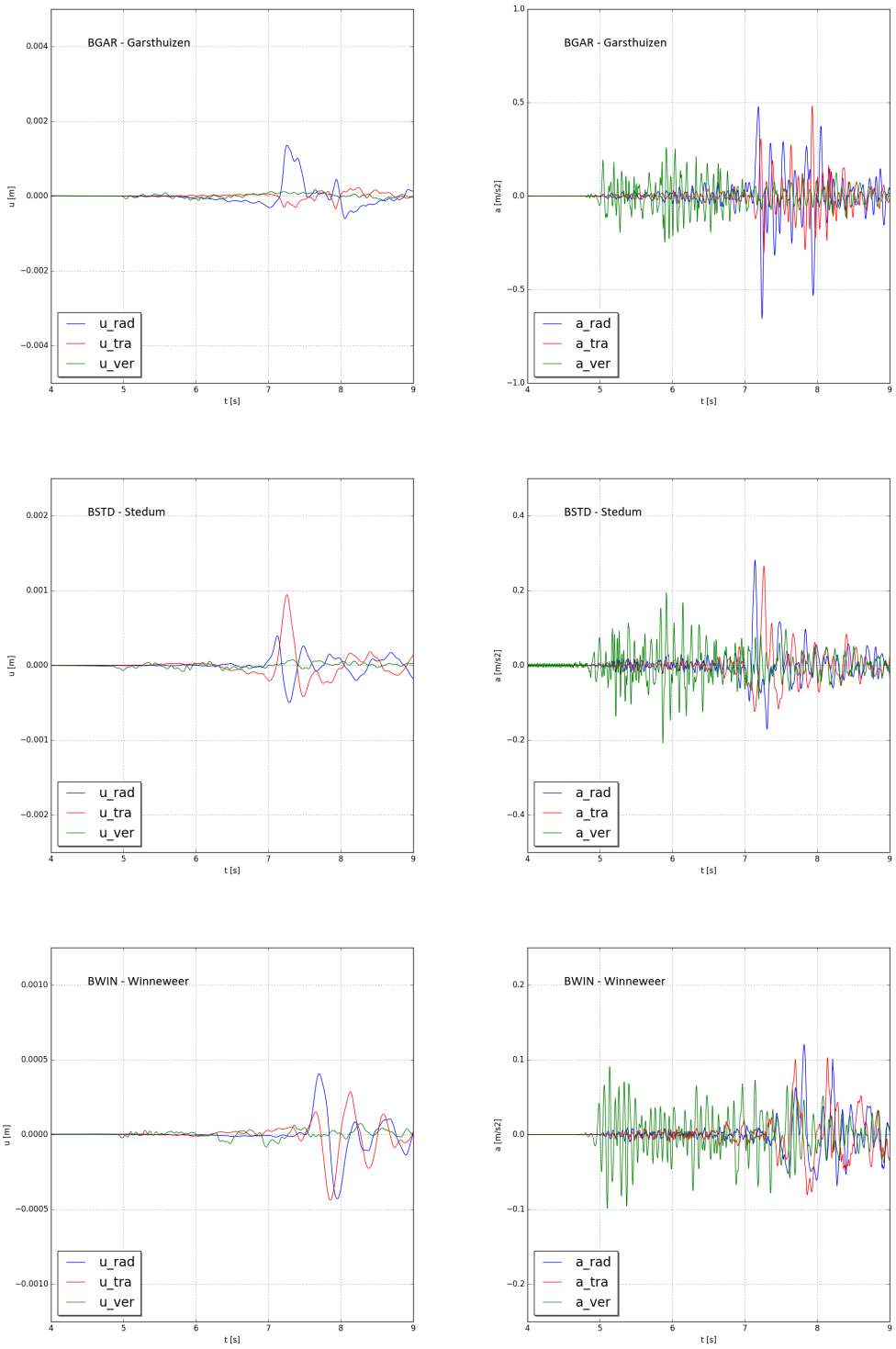


Figure A.5 : Displacements (left) and accelerations (right) of the Garsthuizen, Stedum and Winneweer accelerometers following from the Huizinge tremor. The signals originate from KNMI.
The blue, red and green curves show the radial, transverse and vertical displacements, $u_{rad}$, $u_{tra}$ and $u_{ver}$ and corresponding accelerations $a_{rad}$, $a_{tra}$ and $a_{ver}$, respectively.

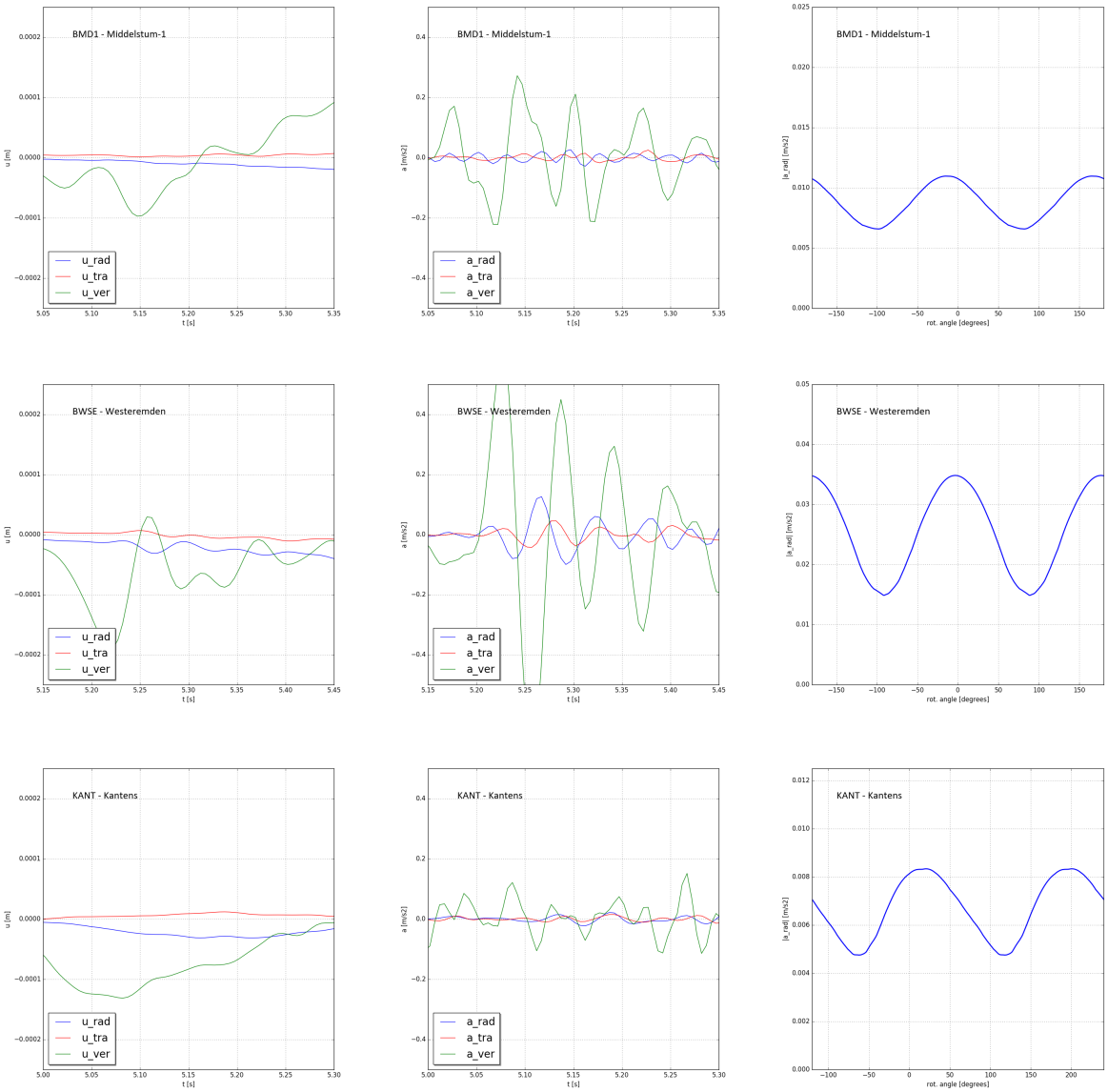


Figure A.6 : Displacements (left), accelerations (centre) and mean rms values of the amplitude of the radial accelerations $|a_{rad}|$ during the passage of the P wave as a function of the horizontal rotation of the accelerometer with respect to the rotation determined by KNMI (right). Signals from the Middelstum, Westeremden and Kantens accelerometers following from the Huizinge tremor.
The blue, red and green curves show the radial, transverse and vertical displacements, $u_{rad}$, $u_{tra}$ and $u_{ver}$ and corresponding accelerations $a_{rad}$, $a_{tra}$ and $a_{ver}$, respectively. Some low-frequency drift in the displacements is due to electronic disturbances.

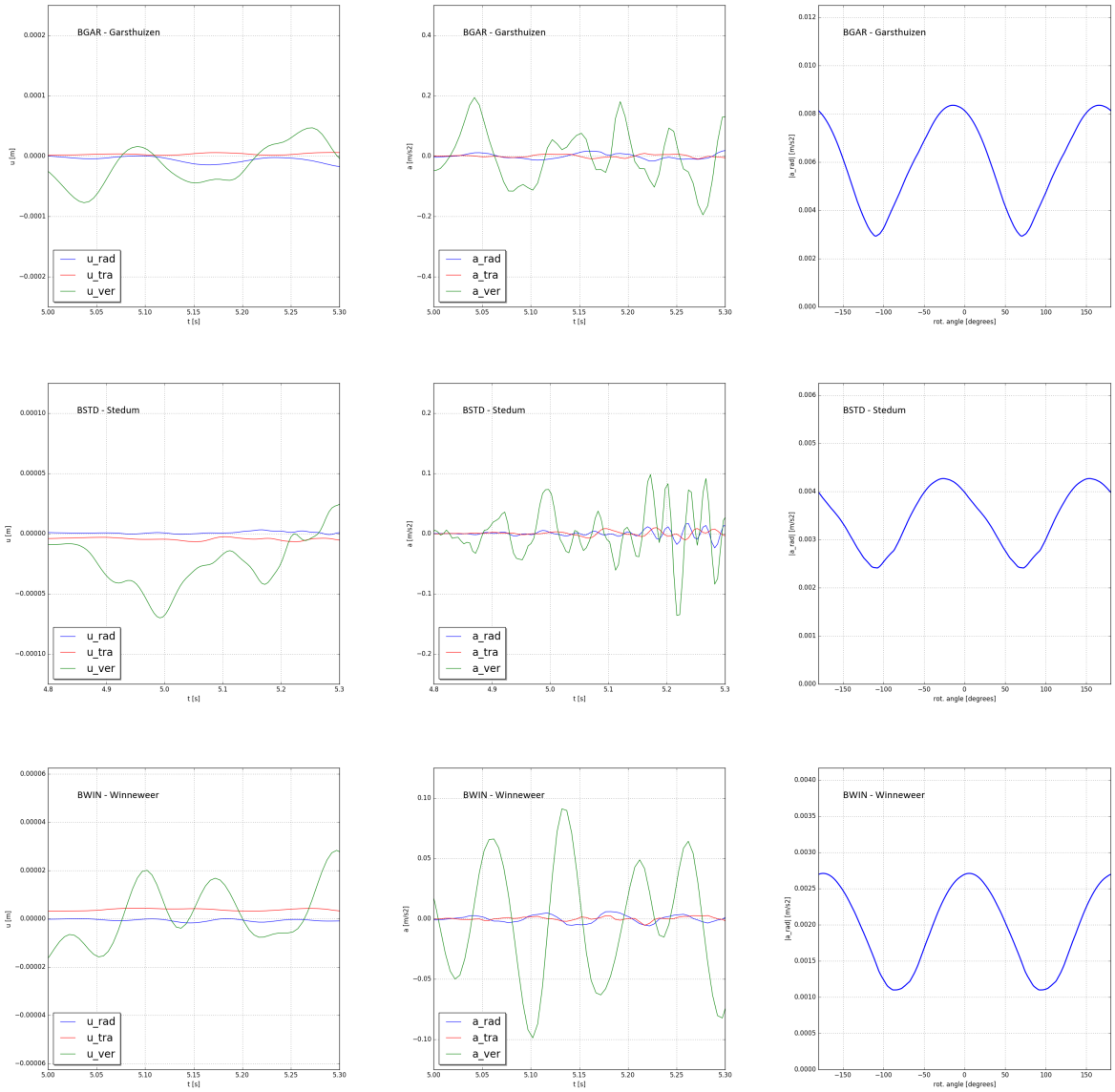


Figure A.7 : Displacements (left), accelerations (centre) and mean values of the amplitude of the radial accelerations $|a_{rad}|$ during the passage of the P wave as a function of the horizontal rotation of the accelerometer with respect to the rotation determined by KNMI (right). Signals from the Garsthuizen, Stedum and Winneweer accelerometers following from the Huizinge tremor.
The blue, red and green curves show the radial, transverse and vertical displacements, $u_{rad}$, $u_{tra}$ and $u_{ver}$ and corresponding accelerations $a_{rad}$, $a_{tra}$ and $a_{ver}$, respectively. Some low-frequency drift in the displacements is due to electronic disturbances.

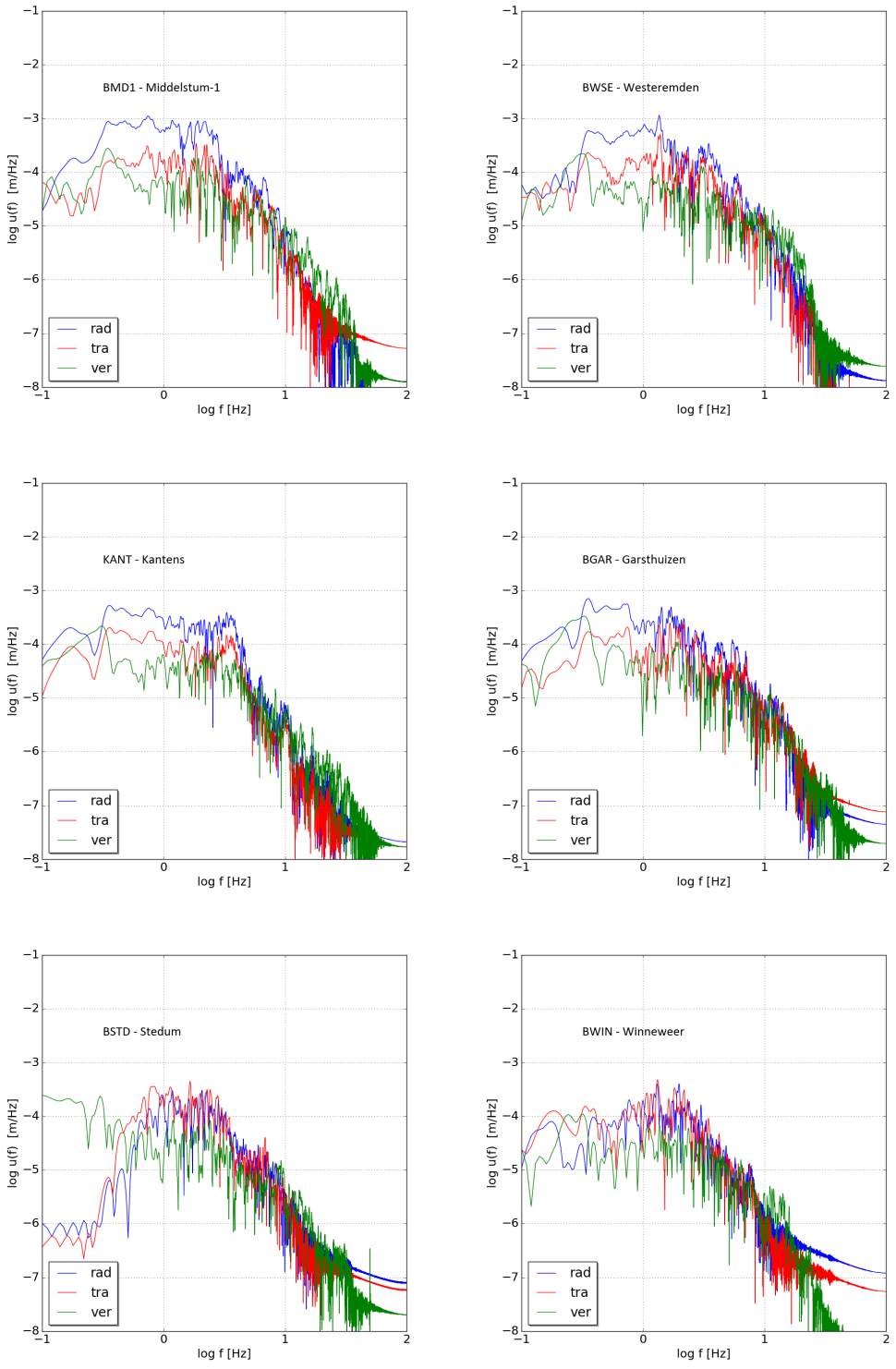


Figure A.8 : Absolute values of Fourier transforms of the displacements (left). The blue, red and green solid curves show the Fourier transforms of the radial, transverse and vertical displacement components, respectively.

# Appendix A.3 Ground accelerometer recordings of recent tremors

There is a problem in reconstructing the orientation of the ground accelerometers in the horizontal plane from the mean rms amplitude of the radial accelerations during the passage of the P wave $|a_{rad}|$. This problem becomes clear from observed signals of several recent tremors in the Groningen field. These tremors are strong enough to generate signals significantly above the noise floor of the receivers and small enough to treat them as point sources.
Not far from the epicentres of these tremors, there are several seismological stations which are part of the recently expanded seismological network of KNMI in the north-east part of the Netherlands. These stations are equipped with a ground accelerometer at the surface and four geophones located in a shallow borehole at 50, 100, 150 and 200 m depth below the accelerometer. For the stations listed, the orientations of the ground accelerometers and downhole geophones are known[5].

Figure A.9 shows the tremor epicentres, the faults around them and the nearby KNMI stations which we have selected for signal analysis. Table A.6 lists the coordinates of the tremor epicentres and KNMI stations.

The signals are extracted from so-called Mini-SEED files which can be obtained from KNMI's Website "Seismic and Acoustic Data Portal". The signals have been filtered with an additional 2 Hz, 2nd order high-pass filter to suppress artificial electronic disturbances in the signals. Figure A.10 shows three typical displacement signals obtained from the downhole geophones and ground accelerometers at various distances from the tremor epicentres. The figures zoom in on the arrival of the P wave and show $|a_{rad}|$ as a function of the horizontal rotation of the accelerometers.
The $|a_{rad}|$ values of the downhole geophones are in general maximal during the passage of the P wave and, consequently, the corresponding rms value of the transverse component

[5]In general, the ground accelerometers have been oriented with respect to the north direction according to installation instructions. Recently, the orientation of the ground accelerometers have been checked by KNMI using the seismic waves from the M 8.1 earthquake which struck off the Pacific Coast of Mexico around 87 km south-west of Pijijiapan on 7 September 2017, in the frequency range of 0.05 - 0.3 Hz. For most of the accelerometers, there are minor deviations of less than $\pm$ 20° in the orientations according to installation instructions, from non published data November 2017, Elmer Ruigrok (KNMI), see also Table A.6 .
Most of the stations are within a distance of 10 km from the tremor epicentres. For a few tremors we have analysed data from stations farther away. For these stations, we are able to decide whether the shallow subsurface generates more multiples.

The geophone orientations have been partly determined by explosive check shots. The collaborative results from NAM, SGS-I and KNMI are shared in an Excel workbook which is regularly updated. The orientations used in this report are the KNMI ones from the October 2017. The vertical component of the geophones, which is defined as positive in the downwards direction, has been reversed as positive in upwards direction, like for the ground accelerometers.

$|a_{tra}|$ values are minimal, leading to negligible transverse displacements. In particular, this holds for the deeper geophones at 200, 150 and 100 m depth. This is not the case for the ground accelerometers[6]. Significant differences are observed. This arises doubts whether the method which reconstructs the orientation of the ground accelerometers recording the Huizinge tremor from maximising $|a_{rad}|$, is robust.

Table A.7 lists the rotations required to maximise $|a_{rad}|$ for the ground accelerometers. Most times, these rotations well exceed rotational adjustments of the ground accelerometers based on recent calibrations by KNMI, see Table A.6 . Using the ground accelerometer orientations according to installation procedures, relatively strong transverse ground displacements are observed during the passage of the P wave[7]. Likely, the P wave, which is primarily in vertical direction, scatters part of its energy in horizontal directions and herewith also in the transverse direction.

- In several cases, multiple oscillations are recorded during the passage of the S wave by the ground accelerometer but not by downhole geophones below them, see also Table A.7 and Figure A.11 [8].
- The damping of S waves in the shallow subsurface is in most cases moderate. This can be concluded from the reduction of the amplitude of direct body waves reflected at the surface and propagating downwards. In general, the reduction is 10 - 30%.
- From intersections of the low- and high-frequency asymptotes in the Fourier spectra of the displacements, we can estimate the so-called corner frequencies $f_c$ [Hz] of the tremors. For most stations, $f_c$ varies in the range 6 - 12 Hz. The high-frequency asymptotes of the spectra decay roughly with $f^{-n}$ with $n$ in the range 2 - 3. From a simple estimate for circular rupture planes, the slip plane radii are in the range 50 - 100 m. The related breakdown stress drop $\Delta\tau$ [Pa] is of the order 1 MPa[9]. This is in the range of expected values for the Groningen field according to Kraaijpoel and Dost (2013).

[6]Also, a horizontal rotation of the ground accelerometer to maximise $|a_{rad}|$ for one tremor does not lead to a maximal $|a_{rad}|$ for the same rotation of the ground accelerometer for another tremor.

[7]Corrections for these deviations have not been used in this report because the data is preliminary and does significantly and systematically increase $|a_{rad}|$.

[8]The same can be concluded when the ground accelerometer signals are filtered by an additional 4.5 Hz high-pass filter to mimic the response function of the downhole geophones. The multiples deform but remain.

[9]For a circular slip plane with radius $R$ [m], the seismic moment relates to the breakdown stress $\Delta\tau$ [Pa] as, see for example Scholz (2002), Eq. 4.30, $M_0 = 16/7\Delta\tau R^3$ and vice-versa $\Delta\tau = 7/16 M_0/R^3$. The radius $R$ follows from $R \sim C' \frac{V_s}{f_c}$ where $C'$ [-] is a constant, $V_s$ [m/s] is the S wave velocity in the rock around the source and $f_c$ [Hz] is the corner frequency. $C' \sim 0.37$, according to Udias et al. (2014), Eq. 9.27. This value is somewhat higher than the value $C' \sim 0.28$ derived by Sato and Hirasawa for a circular slip plane, see Aki and Richards (2009), §10.1.7, Eq. 10.35. We use $R \sim 0.3 V_s/f_c$ where $V_s \sim 2.2$ km/s, see also Wentinck (2017), Appendix D. A more accurate value for $\Delta\tau$ cannot be given, considering the wide range of corner frequencies and uncertainty in the rupture velocity.

- The Appingedam $M_L$ 1.8 tremor consists of two slip events about 1 s after each other[10]. The ground accelerometers signals of the first slip event, which is much weaker than the second slip event, are too noisy to determine $|a_{rad}|$ for the P wave as a function of rotation. Further, the S wave of the first slip event mix with the P wave of the second event. For this tremor, it is also not possible to determine $|a_{rad}|$ for the P wave of the second slip event.

[10]The location of station G67 is almost on top of the hypocentre of this tremor. For this reason, it cannot be used for P wave orientation. The difference between the arrival times of P and S waves is either $\Delta t_{PS} \sim 1.3$ s or $\Delta t_{PS} \sim 2.5$ s. According to the ray tracing method, using the velocity model shown in Figure A.1 in §A.4, the hypocentre of this tremor either at reservoir depth or at more than 5 km deep. The latter seems not realistic.

Table A.6 : Recent tremors in the Groningen field. The Dutch Rijksdriehoeksstelsel (RD) coordinates of the tremors and the KNMI stations. The stations are used to determine the rms values of the radial accelerations on the ground during the passage of the P wave $|a_{rad}|$ and the occurrence of multiple oscillations on the ground during the passage of the S wave.
The numbers between brackets behind the station names are orientations of the ground accelerometers with respect to the north direction in degrees, as determined in November 2017 by Elmer Ruigrok (KNMI) from seismic, non-published data. In general, deviations from north are minor except for station G49. Station G54 is not calibrated. For stations G35, G45 and G49 only the orientations of geophones G352, G354, G451, G452, G453, G491, G492 and G493 have been calibrated.

| name | KNMI station | date | $M_L$ | X | Y |
|---|---|---|---|---|---|
| | | | Richter | m | m |
| tremors | | | | | |
| Froombosch | G34, G44, G49, G54 | 2016-02-25 | 2.4 | 248172 | 578382 |
| Muntendam | G50, G51, G54 | 2016-03-25 | 1.8 | 256270 | 574872 |
| Schildwolde | G40, G41, G45 | 2016-09-02 | 2.1 | 252306 | 582249 |
| Wirdum | G19, G23, G24, G67 | 2016-11-01 | 1.9 | 249653 | 591435 |
| Wirdum | G19, G23, G24, G67 | 2016-11-01 | 2.2 | 249775 | 591994 |
| Loppersum | G19, G23, G24, G67 | 2016-12-07 | 1.8 | 247385 | 594953 |
| Zuidlaren | G45, G49 | 2016-12-23 | 2.4 | 243766 | 567056 |
| Zeerijp | G19, G23, G24, G67 | 2017-03-11 | 2.1 | 246483 | 596828 |
| Woldendorp | G20, G30, G36, G41 | 2017-04-04 | 1.8 | 261993 | 588355 |
| Scharmer | G44, G45, G49 | 2017-04-26 | 2.0 | 243573 | 581189 |
| Overschild | G22, G24, G40 | 2017-05-16 | 1.7 | 249555 | 589652 |
| Slochteren | G35, G40, G41, G45, G46, G50, G51 | 2017-05-27 | 2.6 | 251654 | 581456 |
| Appingedam | G14, G19, G20, G23, G24, G67 | 2017-08-29 | 1.8 | 250606 | 593792 |
| Tjuchem | G24, G30, G35, G36, G67 | 2017-09-05 | 1.9 | 254299 | 589303 |
| stations | | | | | |
| 't Zandt | G14 (4) | | | 247120 | 597795 |
| Oostwijtwerd | G19 (1) | | | 250240 | 595542 |
| Biessem | G20 (17) | | | 255450 | 595371 |
| Stedum | G22 (18) | | | 241007 | 592313 |
| Garrelsweer | G23 (33) | | | 247003 | 592324 |
| Steendam | G24 (24) | | | 252957 | 590273 |
| Meedhuizen | G30 (18) | | | 255581 | 589124 |
| Overschild | G34 (3) | | | 246959 | 585987 |
| Siddeburen | G35 (12) | | | 253431 | 586379 |
| Wagenborgen | G36 (9) | | | 257570 | 587595 |
| Schildwolde | G40 (-7) | | | 250010 | 582986 |
| Noordbroek | G41 (-24) | | | 255493 | 582915 |
| Harkstede | G44 (22) | | | 241644 | 580505 |
| Ruiten | G45 (6) | | | 247036 | 580086 |
| Noordbroek | G46 (18) | | | 252739 | 580009 |
| Kolham | G49 (-76) | | | 244817 | 577481 |
| Sappemeer | G50 (-10) | | | 250084 | 577362 |
| Zuidbroek | G51 (-18) | | | 255135 | 577320 |
| Kielwinde | G54 (not calibrated) | | | 246757 | 571700 |
| Appingedam | G67 (14) | | | 250661 | 593722 |

Table A.7 : Recent tremors in the Groningen field. The third column gives the distances between the stations and the tremor epicentre. The fourth column lists the rounded angles over which the ground accelerometer should be rotated to obtain maximal $|a_{rad}|$ during the passage of the P wave. "–" means that electronic disturbances in the accelerometer signals for the horizontal components are too strong to determine the rotation angle. "all" means that also the geophones have a significant transverse displacement during the passage of the P wave. Note that ground accelerometer rotations required to determine the seismic source parameters can differ multiples of 180 degrees.
The last column lists when multiple oscillations are recorded (yes/no,?) by the accelerometer during the arrival of the S wave of similar magnitude as the first oscillation but not by the geophones below the accelerometer. Data of the stations with names between brackets require another check of the orientation of the ground accelerometer.

| tremor | M | KNMI station<br>distance from tremor in km | required rotation for<br>maximal $\|a_{rad}\|$ in degr. | multiples in S wave |
|---|---|---|---|---|
| ..... | ..... | ..... | ..... | ..... |
| Froombosch | 2.4 | G34, G44, (G49), (G54)<br>7.7, 6.9, 3.5, 6.8 | G34, G44, (G49),(G54)<br>30, 45, 90, -15 | G34, G44, (G49), (G54)<br>?, yes, yes, yes |
| Muntendam | 1.8 | G50, G51, (G54)<br>6.7, 2.7, 10.0 | G50, G51, (G54)<br>–, -45, – | G50, G51, (G54)<br>yes, no, ? |
| Schildwolde | 2.1 | G40, G41, G45<br>2.4, 3.3, 5.7 | G40, G41, G45<br>-45, 90, – | G40, G41, G45<br>no, no, no |
| Wirdum | 1.9 | G19, G23, G24, G67<br>4.1, 2.3, 3.5, 2.5 | G19, G23, G24, G67<br>45, 30, 45, -60 | G19, G23, G24, G67<br>yes, yes, yes, yes |
| Wirdum | 2.2 | G19, G23, G24, G67<br>3.6, 2.8, 3.6, 1.9 | G19, G23, G24, G67<br>–, all, 45, -70 | G19, G23, G24, G67<br>yes, yes, yes, yes |
| Loppersum | 1.8 | G19, G23, G24, G67<br>2.9, 2.7, 7.3, 3.5 | G19, G23, G24, G67<br>-20, -70, –, 30 | G19, G23, G24, G67<br>no, no, yes, no |
| Zuidlaren | 2.4 | G45, (G49)<br>13.4, 10.5 | G45, (G49)<br>90, 90 | G45, (G49)<br>?, ? |
| Zeerijp | 2.1 | G19, G23, G24, G67<br>4.0, 4.5, 9.2, 5.2 | G19, G23, G24, G67<br>-60, -30, -80, – | G19, G23, G24, G67<br>?, yes, yes, no |
| Woldendorp | 1.8 | G20, G30, G36, G41<br>9.6, 6.5, 4.5, 8.5 | G20, G30, G36, G41<br>–,-30, -60, – | G20, G30, G36, G41<br>?, no, no, ? |
| Scharmer | 2.0 | G44, G45, (G49)<br>2.0, 3.6, 3.9 | G44, G45, (G49)<br>-60, -70, – | G44, G45,(G49)<br>no, yes, no |
| Overschild | 1.7 | G22, G24, G40<br>3.5, 9.0, 6.7 | G22, G24, G40<br>–, –, – | G22, G24, G40<br>?, yes, no |
| Slochteren | 2.6 | G35, G40, G41, G45<br>5.2, 2.2, 4.1, 4.8 | G35, G40, G41, G45<br>–, 0, 80, 70 | G35, G40, G41, G45<br>no, no, yes, yes |
| | | G46, G50, G51<br>1.8, 4.4, 5.4 | G46, G50, G51<br>–, 0, -45 | G46, G50, G51<br>no, no, no |
| Appingedam | 1.8 | G14, G19, G20<br>1.8, 4.2, 5.1 | G14, G19, G20<br>30, –, – | G14, G19, G20<br>yes, yes, yes |
| | | G23, G24, G67<br>3.9, 5.3, 0.1 | G23, G24, G67<br>–, –, – | G23, G24, G67<br>yes, yes, yes |
| Tjuchem | 1.9 | G24, G30, G35, G36, G67<br>1.7, 1.3, 3.0, 3.7, 5.7 | G24, G30, G35, G36, G67<br>90, all, 70, -60, -70 | G24, G30, G35, G36, G67<br>no, yes, no, yes, yes |

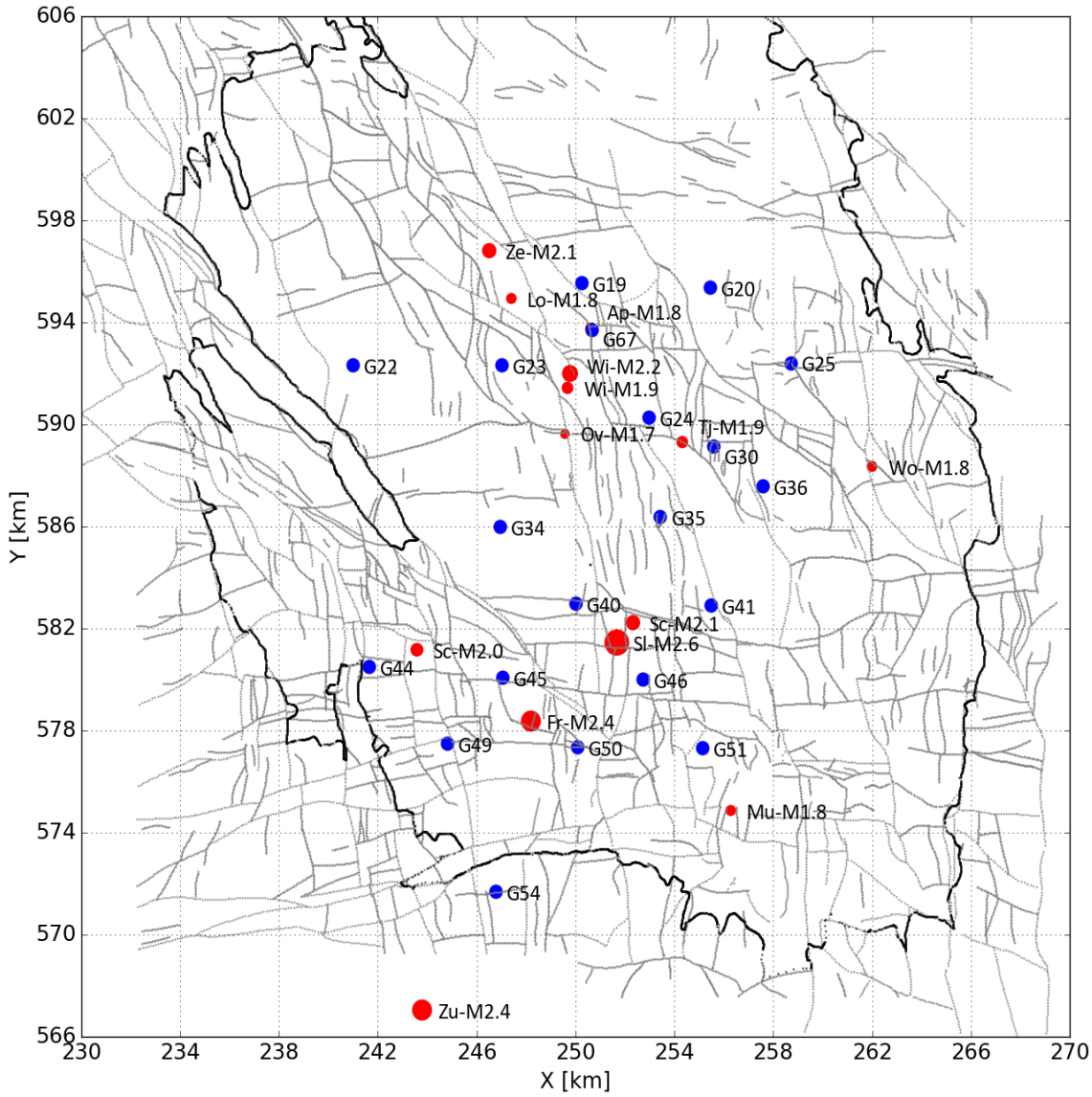


Figure A.9 : Faults and locations of tremor epicentres (red dot) and KNMI stations (blue dots) in the regions around several recent tremors in Dutch Rijksdriehoeksstelsel (RD) coordinates. The areas of the red dots $A$ scale with the tremor magnitudes as $A \propto 10^M$. The tremor names in the map are abbreviated with the first two letters of the location name and the tremor magnitude.
The faults shown are from a NAM database that includes the fault dip, throw and azimuth angles. The thin grey dotted and solid fault lines shown are intersections of the faults with the upper horizon of the Rotliegend reservoir. The RD coordinates of the tremor epicentres and KNMI stations are given in Table A.6 .

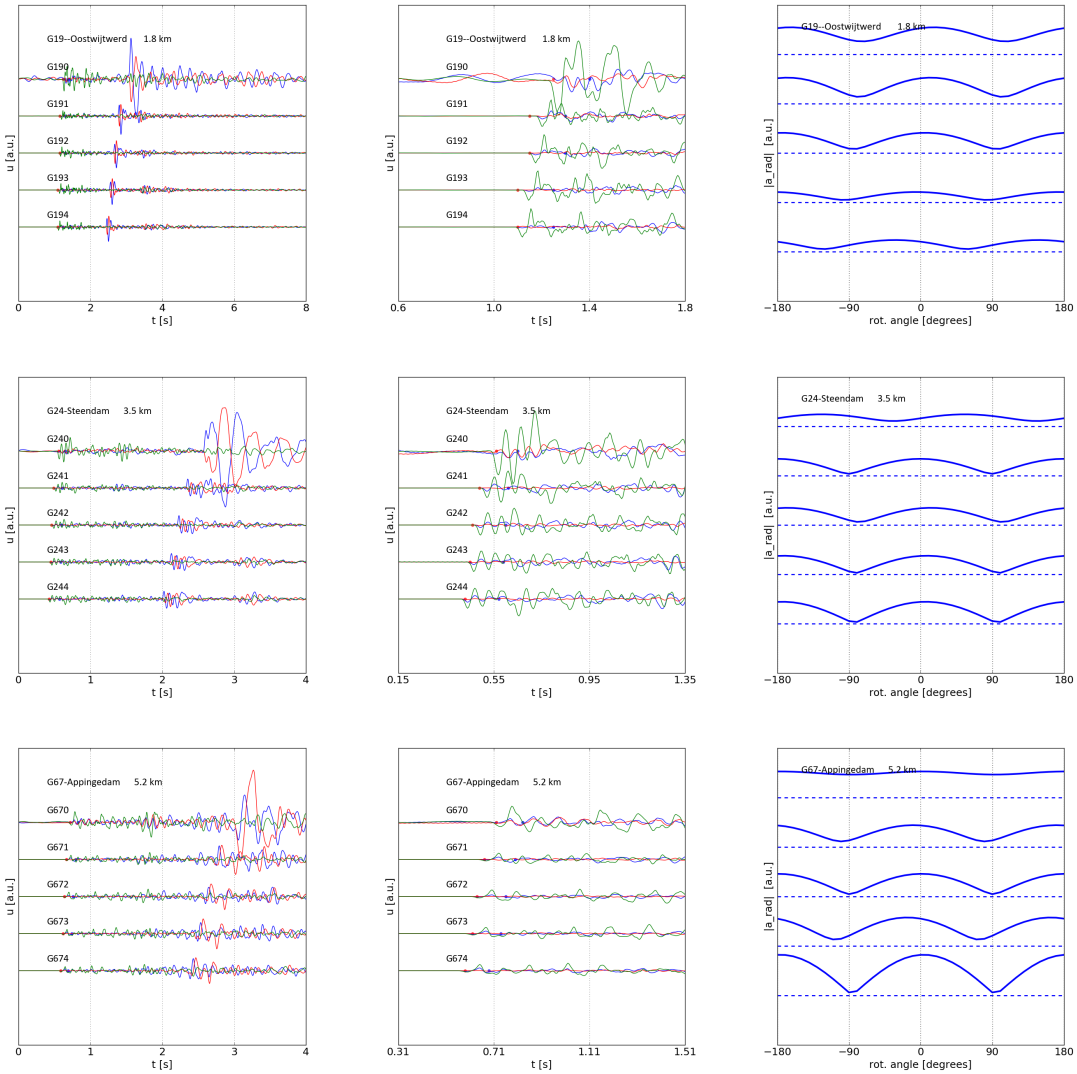


Figure A.10 : Three examples of displacements recorded by KNMI stations comprising 4 downhole geophones at 200, 150, 100 and 50 m depth and a ground accelerometer. The left figures show the signals just after the P wave arrives at the deepest geophone and until the downwards moving S wave from the surface passes the same geophone. The centre figures zoom in on the displacements during the passage of the P wave. The right figures show $|a_{rad}|$ as a function of the horizontal rotation of the sensors with respect to the calibrated orientation. From top to bottom: Appingedam $M_L$ 1.8: station G19 and Wirdum $M_L$ 1.9: station G24, Zeerijp $M_L$ 2.1: station G67.
The blue, red and green curves show the radial, transverse and vertical displacements, $u_{rad}$, $u_{tra}$ and $u_{ver}$. The rotations are with respect to the sensor orientations determined by KNMI. Some low-frequency drift in the displacements are due to electronic disturbances. The start time of the signal is not coupled to the generation of the tremor.

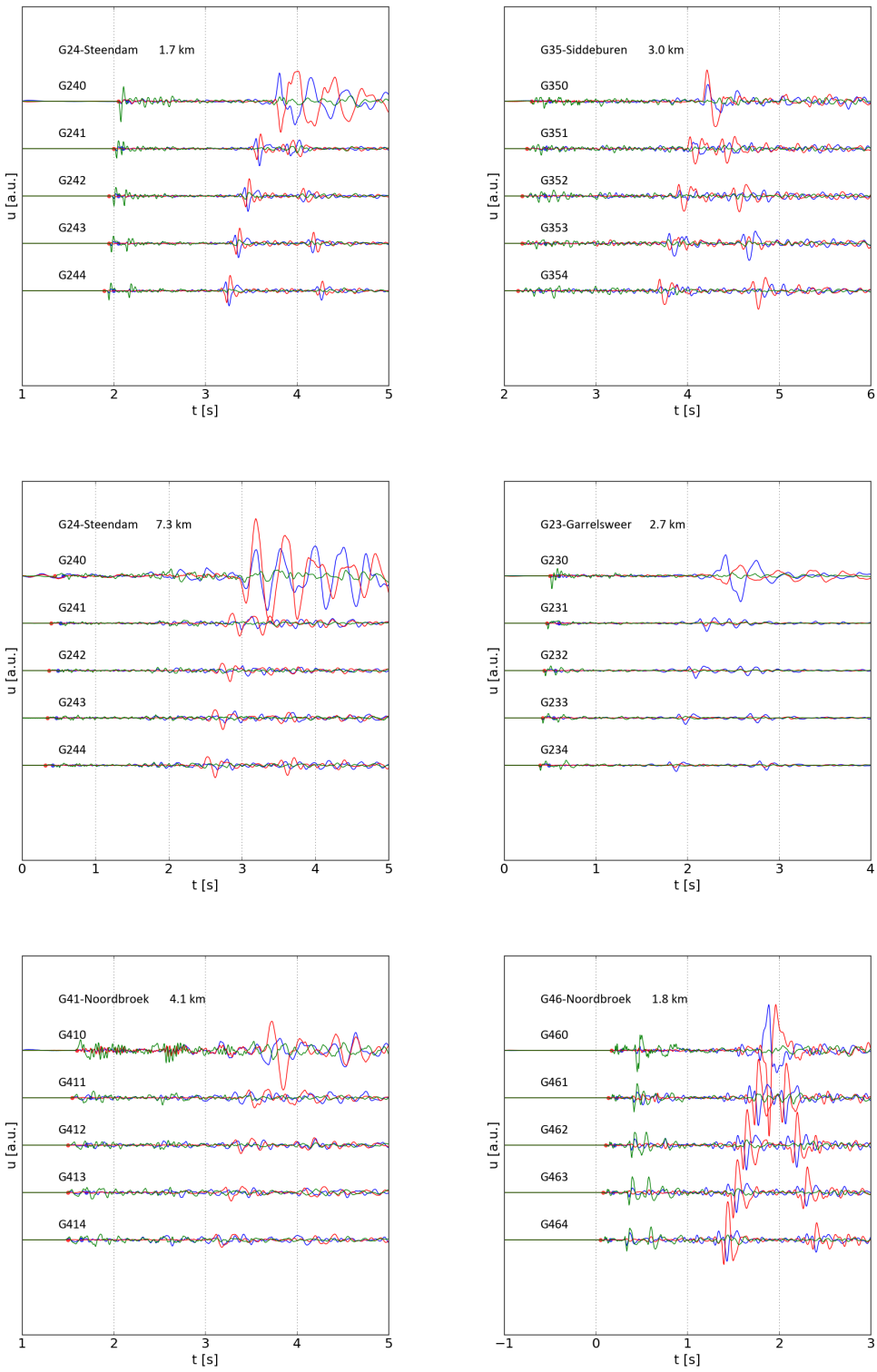


Figure A.11 : Three typical examples of multiple oscillations in the ground motion signals. From top to bottom: Tjuchem $M_L$ 1.9, multiples for station G24 (left) but not for station G35 (right), Loppersum $M_L$ 1.8: multiples for station G24 (left) but not for station G23 (right) and Slochteren $M_L$ 2.4: multiples for station G41 (left) but not for station G46 (right).
The blue, red and green curves show the radial, transverse and vertical displacements, $u_{rad}$, $u_{tra}$ and $u_{ver}$. The rotations are with respect to the sensor orientations determined by KNMI. Some low-frequency drift in the displacements are due to electronic disturbances. The start time of the signal is not coupled to the generation of the tremor.

# Appendix A.4 P and S wave arrivals times

In most cases, displacements peak when the P and S waves pass the ground accelerometers. Without an absolute time line for the Huizinge tremor, the time differences between the peaks could be used to estimate the depth of the hypocentre of this tremor. Since similar peaks also follow from the FEM simulations, the latter can help to select them in the observed signals albeit that the simulations don't include the slow down of the S waves in the shallow subsurface.
In addition, we have calculated travel times of the P and S waves from ray tracing for a point source using a simplified velocity model of the subsurface. Ray tracing is based on standard wave refraction equations for elastic waves passing flat interfaces between rocks with different elastic properties. These include mode conversions from P to S and from S to P waves and the related refraction angles and transmission coefficients, see for example Aki and Richards (2009), §5.2.4. The equations are particularly useful for waves with wavelengths significantly smaller than the thickness of the formations through which the waves propagate.

The simplified velocity model used for the ray tracing calculations has five subsurface formations I-V, see Table A.8 and Figure A.1 . The mean P wave velocity $V_{p,mean,II}$ [m/s] in formation II is calculated from $V_{p,mean,II} = \sum h_{mean,i} / \sum (h_{mean,i}/V_{p,mean,i})$. Herein, $h_{mean,i}$ [m] and $V_{p,mean,i}$ [m/s] are the mean thickness and the mean P wave velocity in formation $i$, respectively. The summation is over all subsurface formations in formation II, i.e., the anhydrite, lower Zechstein, floater and upper Zechstein formations. $V_{p,mean,i}$ is calculated from $V_{p,mean,i} = h_{mean,i}^{-1} \int V_p^{-1}(z)dz$ where the integration is over the depth of formation $i$.
Similar equations apply for formations II and V and for the S wave velocities in these formations. The S wave slow down in the shallow subsurface in formation V can be included by adjusting $V_s(z)$ in the Upper North Sea formation.

Figure A.12 shows the P and S wave arrivals as a function of distance from the Huizinge tremor epicentre from ray tracing and from FEM simulations. The simulated P wave arrives about 0.2 s later than the one from ray tracing. The simulated S wave arrives about 0.4 s later than the one from ray tracing. Part of these differences can be explained from the extent of the seismic source. It takes about 0.25 seconds before the rupture reaches the end of the defined slip plane (and it takes about 0.08 s before the source time function in the slip patches reaches a maximum value). So far, the additional delay in the arrival of the S wave is not clear[11].
The simulated time difference $\Delta t_{PS}$ between the peaks in the signals indicating the passage of P and S waves correspond fairly well with the observed time differences. So, the assumption of a tremor hypocentre at 3 km depth is not inconsistent with the observations. The accuracy of the depth estimation is moderate because the P and S wave arrival

[11]It could be related to simplifications in the ray tracing model, e.g. ignoring the wave velocity gradient in the chalk and lumping the floater and anhydrite in the Zechstein into one formation.

times cannot be easily determined in the observed signals and because the aperture of the small number of receivers in vertical direction is limited. In this case, the depth of the tremor hypocentre could easily differ a few hundred metres.

Figure A.13 shows similar plots for two recent tremors, using the mean depth and thickness of the formations in those regions. For these tremors, we use the signals of the geophones at 200 m depth. The observed and calculated time differences from ray tracing match quite well for these point sources for tremor hypocentres at 3 km depth. With some uncertainty in the determination of the arrival times, we estimate the accuracy of the tremor hypocentre depth for these two recent tremors ± 0.2 km.

Table A.8 : Formations used in a simplified subsurface model for ray tracing calculations for the Huizinge tremor. The depths of the lower horizons of formations I - V are equal to the mean depth of the lowest subsurface formation that is included in this formation. The mean P and S wave velocities in formations I - V are also shown by the dashed lines in Figure A.1 .
S wave slow down in the shallow subsurface (in the North Sea formations) reduces $V_{s,mean}$ in formation V from 687 m/s to 609 m/s.

| Formation | Formations included | depth lower horizon m | $V_{p,mean}$ m/s | $V_{s,mean}$ m/s |
|---|---|---|---|---|
| V | Upper North Sea<br>Lower North Sea | -850 | 2035 | 687/609 |
| IV | Chalk | -1690 | 3509 | 1691 |
| III | Rijnland<br>Altena<br>Triassic | -1935 | 3384 | 1830 |
| II | upper Zechstein<br>floater<br>lower Zechstein<br>anhydrite | -2876 | 4539 | 2558 |
| I | Rotliegend reservoir | -3144 | 3800 | 2232 |

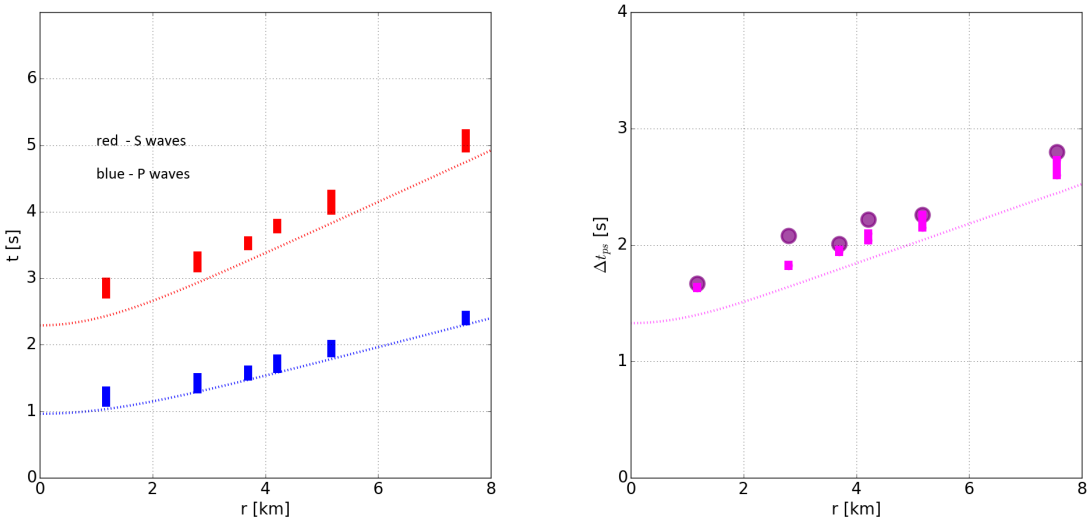


Figure A.12 : Huizinge tremor. Left: arrival times of P and S waves according to FEM simulations (dots) and according to ray tracing (dotted lines) as a function of distance from the tremor epicentre $r$ [m] for a hypocentre at 3 km depth.
Right: calculated and observed time difference $\Delta t_{PS}$ as a function of the distance from the tremor epicentre. The large purple dots show the observed time differences at the station locations. The stations, ordered along the distance from the tremor epicentre, are Middelstum, Kantens, Westeremden, Garsthuizen, Stedum and Winneweer at 1.2, 2.8, 3.7, 4.2, 5.2 and 7.6 km, respectively.

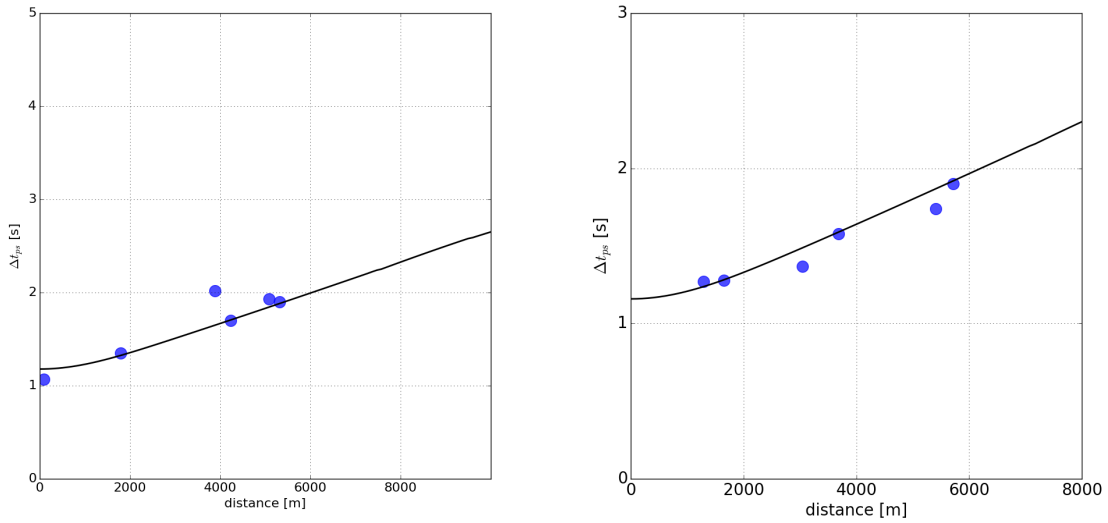


Figure A.13 : Calculated and observed time difference $\Delta t_{PS}$ as a function of the distance from the tremor epicentre $r$ for the Appingedam $M_L$ 1.8 (left) and Tjuchem $M_L$ 1.9 (right) tremors.

# Appendix B

# Seismic source

A seismic source can be modelled as a point source or as an extended source. For a point source, the kinematics of the rupture process is completely defined by the so-called source time function. This function defines the relaxation of the elastic forces on the slip plane as a function of time. In this case, the dimensions of the slip plane and the rupture velocity are indistinguishable and implicitly included in the dynamics of the source time function.

For an extended source, the rupture velocity and the dimensions of the slip plane are explicitly included in the seismic source model. In general, the slip plane is divided in a number of relatively small slip patches. For each slip patch a source time function is defined, which is in general a function of space and time. To model an extended source along fault strike, we have divided the rupture plane in a number of slip patches along fault strike. The source time functions, representing the slip rate for each slip patch, are all the same except for a time shift. The time shift is defined by the rupture velocity, see §B.2.

## Appendix B.1 Source time functions

We assume that the reservoir rock is uniform and isotropic and the slip on the fault plane is only deviatoric. For a receiver at a large distance from the seismic source, the source can be represented by a point source with a double couple or with a moment tensor[1]. The time dependent moment tensor $\boldsymbol{M} = \boldsymbol{M}(t)$ [N] can be factorised in a unit moment tensor $\boldsymbol{m}$ [-][2] and a source time function $M_0(t)$ [N]. The unit moment tensor $\boldsymbol{m}$ [-] is constructed

[1]The source tensor provides fundamental information on the event magnitude, source geometry (e.g. possible fault plane orientations and slip directions), and partitioning among various deviatoric and isotropic motion components. If the reservoir rock is uniform and isotropic, the moment tensor and the so-called potency tensor differ only by a factor equal to the shear modulus $\mu$, see for example Zhu and Ben-Zion (2013). One of the authors notes that, in general, it is better to use the strain-based potency tensor than the stress-based moment tensor, since the potency involves only directly observable quantities whereas the moment requires making assumptions on elastic properties at the source. In this case, this is not needed.

[2][-] means that the property, in this case $\boldsymbol{m}$ is dimensionless or has no unit.

from the unit vectors defining the orientation of the rupture plane and the slip direction, see e.g. Aki and Richards (2009), §3.3. So,

$$\boldsymbol{M}(t) = \boldsymbol{m} M_0(t). \tag{B.1.1}$$

Using the mean relative displacement or slip $D = D(t)$ over the slip plane as the time-dependent variable and the general relation between slip and seismic moment $M_0 = \mu S D$, the seismic moment changes with time as

$$M_0(t) = \mu S D(t) = M_0 f(t) \quad \text{where} \quad D(t) = D_{max} f(t) \quad \text{and} \quad M_0 = \mu S D_{max}. \tag{B.1.2}$$

$D_{max}$ [m] is the maximum value of the mean slip over the slip plane over time. $S$ [m$^2$] is the surface of the slip plane and $\mu$ [Pa] the shear modulus of the rock. $f$ [-] is the dimensionless source time function. From two-dimensional dynamic rupture modelling, we apply the following time derivative $\dot{f} = df/dt$ of the source time function, see Wentinck (2017),

$$\dot{f}(t) = g(t) \frac{t}{t_r^2} \exp(-(t/t_r)^n) \quad \text{where} \quad g(t) = c \frac{t^2}{t^2 + t_{onset}^2}. \tag{B.1.3}$$

$t_r$ [s] is the so-called rise time. $n$ [-] is a shape parameter which determines the decay time of $\dot{f}$. $c$ [-] is a constant, so that $f \to 1$ for $t \gg t_r$. The function $g(t)$ ensures that $f(t)$ has a zero second order time derivative at $t = 0$, which is convenient for the numerical simulations. $t_{onset}$ [s] is a typical time in which $g(t)$ increases from 0 to 1. Using $t_{onset} \ll t_r$, $g(t)$ has a minimum effect on the main shape of the source time function. Figure B.1 shows typical source time functions, including the one used in this report

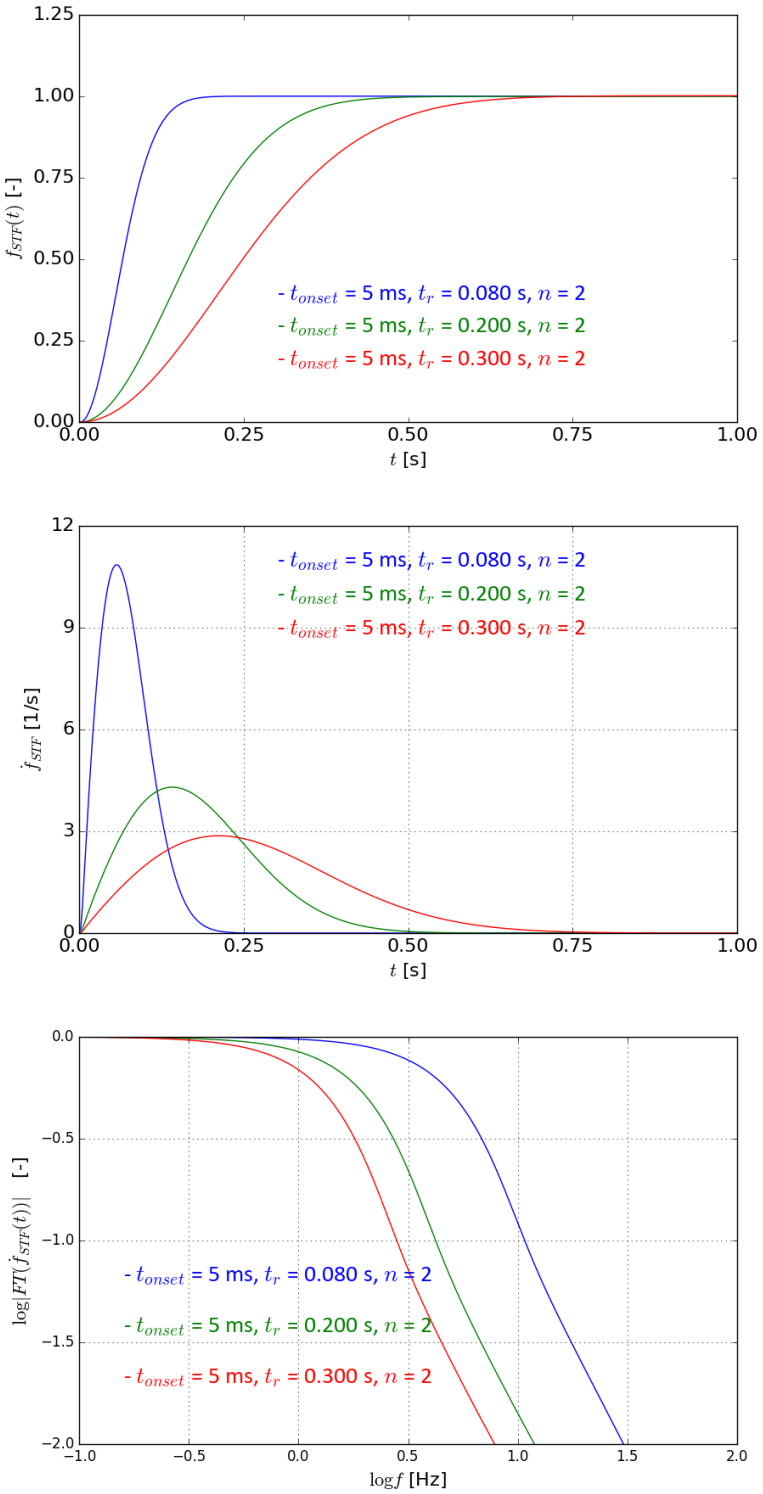


Figure B.1 : Source time function $f(t)$ (top), time derivative $\dot{f}(t)$ (centre) and absolute values of the logarithm of the Fourier transforms of the time derivative $\log^{10}|F(\dot{f}(t))|$ (bottom).
The shape parameters are $n = 2$, $t_{onset} = 5$ ms and $t_r = 0.08$ s (blue), 0.2 s (green) and 0.3 s (red). The corresponding corner frequencies are 5.2, 2.1 and 1.4 Hz, respectively. In all cases, the small onset time $t_{onset}$ has a negligible effect on the shapes of the curves. For the slip patches along fault strike we use the parameters $n = 2$, $t_{onset} = 5$ ms and $t_r = 0.08$ s.

# Appendix B.2 Dimensions of seismic source

The seismic source is represented by a series of double couples with a double couple arm $l_{DC} = 80$ m over a length $L$ of about 1 km. The rupture starts at the source hypocentre and propagates bi-directional, i.e., in both horizontal directions along fault strike with a rupture velocity along fault strike $V_{r,strike} = 2$ km/s, which is 80 - 90% of the S wave velocity in the reservoir. The rupture velocity is the velocity with which the rupture front propagates along the fault plane[3]. The external source model resembles Haskell's model for an extended source, see e.g. Udias et al. (2014), §7.2 or Aki and Richards (2009), §10.1.5.

The source time function for double couple or slip patch $i$ in the series of double couples along fault strike is, using Eq. (B.1.3)

$$\dot{f}_i(t) = g(t_i^*)\frac{t_i^*}{t_r^2}\exp(-(t_i^*/t_r)^n), \tag{B.2.1}$$

where $t_i^* = 0$ for $t < t_{trigger,i}$ and $t_i^* = t - t_{trigger,i}$ for $t \geq t_{trigger,i}$ and the trigger time $t_{trigger,i}$ [s] is given by[4]

$$t_{trigger,i} = \frac{|\boldsymbol{\zeta}_i - \boldsymbol{\zeta}_{nucl}|}{V_{r,strike}}. \tag{B.2.2}$$

$|\boldsymbol{\zeta}_i - \boldsymbol{\zeta}_{nucl}|$ is the distance between double couple $i$ and the centre of the source where the rupture starts. $V_{r,strike}$ [m/s] is the rupture velocity along fault strike.
The modified source time function used has shape parameters $t_r = 0.08$ s, $n = 2$. For these parameters, the time in which the rupture propagates along fault dip is about 0.15 s, see Figure B.1 . This time is sufficient to propagate over a depth of about 0.3 km in one direction for a rupture velocity $V_r = 2$ km/s.

According to Stein and Wysession (2003), §4.6.3, Eq. 20, the breakdown stress drop $\Delta\tau$ [Pa] follows from[5]

$$\Delta\tau \sim \frac{8}{3\pi}\frac{M_0}{WL^2}. \tag{B.2.3}$$

$W$ [m] is the width of the rupture plane along fault dip. $L$ [m] is the length slip plane along fault strike. $M_0$ is the sum of the seismic moments released by all double point sources. If $W$ and $L$ are proportional to the corner frequency $f_c$, this expression shows that the breakdown stress drop is quite sensitive to the corner frequency.

[3]The rupture velocity essentially differs from the so-called slip velocity. The latter one is the relative velocity with which one side of the fault plane fault moves with respect to the other side of the plane. The slip velocity is usually in the order of 1 m/s and is determined by stress breakdown and rock inertia.

[4]With a focus on the low-frequency content of the simulated waves, we disregard irregularities in the rupture velocity along fault strike due to fault roughness and stress variations. To include them, see for example Graves and Pitarka (2010) or Graves and Pitarka (2015).

[5]See also Wentinck (2017), Appendices C and D for details.